The optical characteristics and sources of chromophoric dissolved organic matter (CDOM) in seasonal snow of northwestern China

Yue Zhou[1], Hui Wen[1], Jun Liu[1], Wei Pu[1], Qingcai Chen[2, 3], and Xin Wang[1]

[1] Key Laboratory for Semi-Arid Climate Change of the Ministry of Education, College of Atmospheric Sciences, Lanzhou University, Lanzhou 730000, China

[2] School of Environmental Science and Engineering, Shaanxi University of Science and Technology, Xi'an 710021, China

[3] Graduate School of Environmental Studies, Nagoya University, Nagoya 464-8601, Japan

Correspondence to: Xin Wang (wxin@lzu.edu.cn) and Qingcai Chen (chenqingcai666@163.com).

Abstract.

Chromophoric dissolved organic matter (CDOM) plays an important role in the global carbon cycle and energy budget, but is rarely studied in seasonal snow. A field campaign was conducted across northwestern China from January to February 2012, and surface seasonal snow samples were collected at 39 sites in Xinjiang and Qinghai provinces. Absorption and fluorescence spectroscopies along with chemical analysis were used to investigate the optical characteristics and potential sources of CDOM in snow. The abundance of CDOM (shown as the absorption coefficient at 280 nm, a_{280}) and the spectral slope from 275 to 295 nm ($S_{275\text{-}295}$) ranged from 0.15-10.57 m^{-1} and 0.0129-0.0389 nm^{-1}, respectively. The highest average a_{280} (2.30 ± 0.52 m^{-1}) was found in Qinghai and the lowest average $S_{275\text{-}295}$ (0.0188 ± 0.0015 nm^{-1}) indicated that the snow CDOM in this region had strongly terrestrial characteristic. Relatively low regional averages of a_{280} were found at sites located to the north of the Tianshan Mountains and northwestern Xinjiang along the border of China (0.93 ± 0.68 m^{-1} and 0.80 ± 0.62 m^{-1}, respectively). Parallel factor (PARAFAC) analysis identified three types of fluorophores that were attributed to two humic-like substances (HULIS, C1 and C2) and one protein-like material (C3). C1 was mainly from soil HULIS, C3 was a type of autochthonously labile CDOM, while the potential sources of C2 were complex and included soil, microbial activities, anthropogenic pollution, and biomass burning. Furthermore, the regional variations of sources for CDOM in snow were assessed by the analyses of chemical species (e.g., soluble ions), fluorescent components and air mass backward trajectories combined with the satellite active fire locations.

1 Introduction

Dissolved organic matter (DOM) is widely distributed in natural aquatic ecosystems and plays a key role in the global carbon cycle (Massicotte et al., 2017). Chromophoric dissolved organic matter (CDOM), widely known as the light-absorbing constituent of DOM, can absorb light from ultraviolet to visible (UV-vis) wavelengths (Bricaud et al., 1981). Due to its light-absorbing properties, CDOM is important in biological processes (Seekell et al., 2015; Thrane et al., 2014), photochemical processes (Helms et al., 2013; Vaehaetalo and Wetzel, 2004), and the energy budget (Hill and Zimmerman, 2016; Pegau, 2002) in natural water bodies.

Compared to the aquatic environments, there were only limited studies evaluating DOM in the cryosphere. Whereas the global glacier ecosystem is a large organic carbon pool and exports approximately 1.04 ± 0.18 TgC yr^{-1} of dissolved organic carbon (DOC) into freshwater and marine environments (Hood et al., 2015). In addition, the glacier-derived DOM shows high bioavailability, and can be a source of labile organic matter for the downstream ecosystems (Hood et al., 2009; Lawson et al., 2014; Singer et al., 2012). The DOM in snow and ice originates from the in-situ microbial processes (autochthonous) (Anesio et al., 2009), as well as is imported from the surrounding terrestrial environments (allochthonous), including soil, vegetations (Bhatia et al., 2010), and anthropogenic activities (Stubbins et al., 2012).

Snowfall is an important carbon and nutrient input for land ecosystems (Mladenov et al., 2012) and a crucial freshwater reservoir (Jones, 1999). Besides, snowpack is also an active field for photochemical (Beine et al., 2011; Domine et al., 2013) and biological

processes (Liu et al., 2009; Lutz et al., 2016). Unlike the aquatic environments, high surface albedo is the most obvious physical property of snow (IPCC, 2013). Once light-absorbing impurities are deposited on the snow surface, the albedo can be significantly reduced, and the regional and global climate are further affected (Hadley and Kirchstetter, 2012). Several field campaigns covering the Arctic, Russia, North America and northern China have been conducted to measure insoluble light-absorbing particles (ILAPs) in snow, for instance, black carbon (BC), insoluble organic carbon (ISOC) and mineral dust (MD) (Doherty et al., 2010, 2014, 2015; Huang et al., 2011; Pu et al., 2017; Wang et al., 2013, 2015, 2017; Warren and Wiscombe, 1980; Ye et al., 2012; Y. Zhou et al., 2017). However, these studies neglected CDOM, which is rarely studied in snow but has been proved as an effective light absorber whether in the atmosphere (i.e., brown carbon, BrC) (Hecobian et al., 2010) or water bodies (Bricaud et al., 1981). To constrain the photochemistry of snow soluble chromophores, Anastasio and Robles (2007) first quantified the light absorption of dissolved chromophores in melted snow samples from the Arctic and Antarctica. They found that in addition to NO_3^- and H_2O_2, approximately half of the light absorption at 280 nm and above was responsible for unknown chromophores, probably organics. After that, Beine et al. (2011) analyzed more than 500 snow samples in Alaska. They exhibited that the contributions of H_2O_2 and NO_3^- to the total absorption within 300-450 nm were slight (combined < 9%); while humic-like substances (HULIS), which is a type of macromolecular organic substances defined for aerosol with certain similar chemical properties to terrestrial and aquatic humic and fulvic substances (Graber and Rudich, 2006), and unknown

chromophores each accounted for approximately half of the total absorption. Recently, several studies have started to focus on the optical properties and radiative forcing of CDOM in glaciers on the Tibetan Plateau. Yan et al. (2016) measured the mass absorption cross section (MAC) of CDOM in snow (1.4 ± 0.4 m^2 g^{-1} on average at 365 nm) at Laohugou glacier, northern Tibetan Plateau, and further calculated the radiative forcing of CDOM which accounted for approximately 10% relative to that of BC. Niu et al. (2018) showed a quite high MAC value of CDOM (6.31 ± 0.34 m^2 g^{-1} on average at 365 nm) for snow and ice samples collected on Mt. Yulong, southeastern Tibetan Plateau. Moreover, it is surprising that the light absorption of CDOM within 330 to 400 nm was approximately 4 times higher than that of BC, although with high uncertainty. In above studies, the CDOM showed significant effects on the energy budget of surface snow and ice on glaciers. Until now, the study of CDOM in snow and ice is still in its infancy, and much more work is imperative to improve our understanding of them. In northern China, the snowpack is affected by more anthropogenic activities or sunlight than those at higher elevation or latitude, thus the effects of CDOM may be more remarkable. Therefore, we conducted a large field campaign to investigate the CDOM in seasonal snow of northwestern China from January to February 2012.

UV-vis absorption and fluorescence spectroscopies are both rapid and effective methods of characterizing the optical properties and sources of CDOM. The absorption coefficient at a certain wavelength within the UV band, for instance, 254 nm, 280 nm or 350 nm (Spencer et al., 2012; Zhang et al., 2010, 2011), usually serves as an indicator

of CDOM abundance. The absorption spectrum of CDOM decreases approximately exponentially with increasing wavelength (Helms et al., 2008), and is usually described by the spectral slope (S) (Twardowski et al., 2004). Helms et al. (2008) used the spectral slope between 275 and 295 nm ($S_{275\text{-}295}$) to investigate the molecular weight and sources of CDOM (terrestrial or marine origin), lower $S_{275\text{-}295}$ values correspond to terrestrial and higher molecular weight CDOM. The fluorescence excitation-emission matrix (EEM) has been widely used to identify the sources and compositions (humic-like or protein-like) of fluorescent DOM (FDOM) in natural waterbodies (Birdwell and Engel, 2010; Coble, 1996; Zhao et al., 2016), rainwater (Y. Q. Zhou et al., 2017), fog water (Birdwell and Valsaraj, 2010) and aerosols (Duarte et al., 2004; Lee et al., 2013; Mladenov et al., 2011). To precisely extract the useful information from the large dataset of EEMs, Bro (1997) successfully applied parallel factor (PARAFAC) analysis to decompose the EEMs into several independent fluorescent components. Due to the great advantages of PARAFAC analysis in interpreting the results of EEMs, this has been a "mainstream" approach in recent natural CDOM studies (Murphy et al., 2013). However, the application of EEM combined with PARAFAC analysis in the cryosphere is scarce. Therefore, we try to employ it to characterize the CDOM in snow.

In this study, for the first time, with the aim of presenting a comprehensive understanding of CDOM in seasonal snow across northwestern China, the samples were subjected to UV-vis absorption, fluorescence, and chemical analyses to investigate the abundances, optical properties, and potential sources of CDOM as well as their spatial distributions.

2 Material and methods

2.1 Sample collection

During January to February 2012, snow samples were collected at 7 sites in Qinghai and 32 sites in Xinjiang, which are located in northwestern China. The distribution of sample sites, which are numbered chronologically, is shown in Fig. 1. Based on Pu et al. (2017), these sites were separated into five regions by their geographical distribution to investigate the spatial variations of CDOM optical properties and potential sources. Region 1 is in the southeastern part of Qinghai with high altitude, and other regions were in Xinjiang. Region 2 is along the Tianshan Mountains; region 3 is located to the north of the Tianshan Mountains and close to the industrial city belt in central Xinjiang. Regions 4 and 5 are in the northwestern and northeastern Xinjiang, respectively, and both along the border of China.

The sample sites were chosen to be upwind and far enough away from roads, railways, cities and villages to minimize the effects of local pollution. Hence, the collected samples can be representative for a wide range of areas. Pictures of several sample sites are shown in Fig. 2. Snow samples were collected every 5 cm from top to bottom at each site, and if there was a melt layer or fresh snow on the top layer, such a sample was collected individually. A pair of two adjacent vertical profiles of snow were gathered ("left" and "right") for assessing the variability of the same snowpack and to enhance the accuracy of the measurements. During this campaign, 13 fresh snow samples that had fallen during the sampling time were collected. In addition, at some

sites, the snow was thin and patchy and the wind was strong; hence, these samples were gathered from snow drifts, and potentially influenced by the deposition of local soil dust (Ye et al., 2012). More details on the sampling methods have been reported previously (Doherty et al., 2010; Wang et al., 2013; Ye et al., 2012).

After being returned to the laboratory in Lanzhou University, all the samples were stored in a freezer at -20℃ or lower for subsequent analysis. Although the previous studies indicated that the freeze-thaw process may lead to biases of the optical properties for DOM samples. For instance, Fellman et al. (2008) reported that there was a decrease of specific ultraviolet absorbance (SUVA) for stream water DOM after frozen, with a median of approximately 8%. A study of peatland DOC found that the change of light absorption at 254 nm after freeze and thaw was less than 5% in median (Peacock et al., 2015). Thieme et al. (2016) assessed the changes of fluorescence properties for several types of DOM samples. The results showed the decreased relative percentages of terrestrial humic-like fluorophores (-3% on average) and humification index (HIX, -2% on average), and the increased percentage of fluvic-like fluorophore (+6% on average). However, various types of DOM in previous studies were shown that their optical properties (light absorption and fluorescence) were not affected significantly by frozen effect, such as ocean water, pore water, spring and cave water (Birdwell and Engel, 2010; Del Castillo and Coble, 2000; Otero et al., 2007; Yamashita et al., 2010). As discussed above, the freeze-thaw process may influence the relative contributions of PARAFAC components slightly, and the effects on a_{280} and fluorescence indices can be neglected.

2.2 Fluorescence measurement

The snow samples were firstly melted under the room temperature. Then, the snow water samples were filtrated using 0.22 μm PTFE syringe filters (Jinteng, Tianjin, China), and stored in prebaked glass vials (450 ℃ for 4 h) at 4 ℃ in a freezer. All the samples were measured for UV-Vis and fluorescence spectroscopies within 24 hours after filtration. The ultrapure water (18.2 MΩ·cm) filtrated by the PTFE syringe filters exhibited no clear fluorescence signal.

The EEMs (n = 78) of surface snow samples were measured by an Aqualog spectrofluorometer system (Horiba Scientific, NJ, USA) in a 1 cm quartz cell. The scanning ranges were 240 to 600 nm in 5 nm intervals for excitation and 250 to 825 nm in 4.65 nm (8 pixels) intervals for emission, with the integrating time of 5 s. An ultrapure water blank was subtracted to remove the water Raman scatter peaks.

The inner filter effect (IFE) of EEM was corrected using the method shown in Kothawala et al. (2013). The fluorescence intensities were calibrated by the Raman peak of the ultrapure water reference at a 350 nm excitation wavelength following the method presented by Lawaetz and Stedmon (2009). The Rayleigh scatter peaks of EEMs were addressed by the EEMscat MATLAB toolbox (version 3) using an interpolation algorithm (Bahram et al., 2006).

PARAFAC is a multi-way method for modeling the data with three- or higher-order arrays (Murphy et al., 2013). For the EEMs, the three dimensions are samples, excitation and emission wavelengths. After PARAFAC analysis, the EEMs can be decomposed into several components with clear chemical interpretations. The details

about the theory of PARAFAC analysis can be found in the Supplement. In this study, the PARAFAC analysis was performed by the DOMFluor toolbox (version 1.7) in MATLAB (Stedmon and Bro, 2008). In addition, because the emission signals were mainly in the range of 250-650 nm, those at longer wavelengths were weak and more likely to be noises, hence, the emission wavelengths longer than 650 nm were not considered into the model. According to the analysis of residual error, split-half method and visual inspection, the 3-component PARAFAC model was selected. The residual error decreased distinctly when the component number increased from 2 to 3 and from 4 to 5 (Fig. S1). Combined with the split-half analysis for 2- to 7-component models, only 2- and 3-component models were validated with the "$S_4C_4T_2$" split scheme (Murphy et al., 2013). Therefore, the 3-component model was chosen here. The fluorescence intensity of each fluorescent component was expressed as F_{max} in Raman unit (RU) (Stedmon and Markager, 2005b). The relative contributions of intensity for components to the total fluorescence are given as %C1-%C3 hereinafter. In addition, three fluorescence-derived indices are widely used to identify the potential sources of CDOM. Zsolnay et al. (1999) presented a HIX to describe the relative humification of DOM. The fluorescence index (FI) is used to identify the sources of DOM from terrestrial or microbial origins (McKnight et al., 2001), and the biological index (BIX) can be an indicator of autochthonous productivity (Huguet et al., 2009). These three indices are calculated by the following formulas:

$$FI = I (Ex = 370, Em = 450) / I (Ex = 370, Em = 499), \quad (1)$$

$$BIX = I (Ex = 310, Em = 379) / I (Ex = 310, Em = 430), \quad (2)$$

$$HIX = I(Ex = 255, Em = 434\text{-}480) / I(Ex = 255, Em = 300\text{-}345), \quad (3)$$

where I is the fluorescence intensity, Ex and Em are short for the excitation and emission wavelengths, respectively. We note that the wavelengths used in the calculation were changed slightly (1 nm or less) due to different instruments.

2.3 UV-vis absorption measurement

The UV-vis absorption spectra (n = 78) of snow samples were derived from 240 to 600 nm in 5 nm intervals while the fluorescence measurements were conducted by an Aqualog spectrofluorometer system (Horiba Scientific, NJ, USA), and an ultrapure water blank was used as a reference. The absorbance of CDOM was assumed to be zero above 550 nm, and the average absorbance between 550-600 nm was subtracted from the whole spectrum to correct the baseline shifts and scattering effects of the measurement. The absorbances of the samples were converted to absorption coefficients using the following equation:

$$a(\lambda) = \ln(10) \cdot A(\lambda) / L, \quad (4)$$

where A is the absorbance of the sample, λ is the wavelength, L is the path length of cuvette (0.01 m), and a is the absorption coefficient (m^{-1}). The abundance of CDOM is presented by the absorption coefficient at 280 nm (a_{280}) (Zhang et al., 2010). The spectral slope between 275-295 nm ($S_{275\text{-}295}$) was determined both by a linear fit and an exponential fit. The exponential fit was performed as Eq. (5) (Twardowski et al., 2004):

$$a(\lambda) = a(\lambda_r)e^{-S(\lambda-\lambda_r)}, \quad (5)$$

where the $a(\lambda_r)$ is the absorption coefficient at a reference wavelength λ_r, S is the spectra slope. The variation of these two fitting methods was approximately 3% on average. Finally, linear fit was adopted due to the higher fitting coefficients. Additionally, if the difference in $S_{275\text{-}295}$ between the linear and exponential methods was higher than 10%, indicating a high uncertainty for absorption measurement, such data were removed. The absorption Ångström exponent (AAE) is used to describe the wavelength dependence of light absorption for aerosol (Bond, 2001), which was also applied to characterize the ILAPs and CDOM in snow and ice (Doherty et al., 2010; Niu et al., 2018; Wang et al., 2013; Yan et al., 2016). The AAEs were calculated using power-law fit as follows:

$$a(\lambda) = K \cdot \lambda^{-AAE}, \quad (6)$$

where a is the absorption coefficient (m^{-1}), K is a constant and λ is the wavelength (from 240 to 550 nm). The R^2 of all the fits ($S_{275\text{-}295}$ and AAE) were higher than 0.9 and most of them were higher than 0.95.

Because the light absorption within the visible wavelengths of some samples were below the detection limit of the spectrometer, 19 of 39 samples were available for the calculation of AAE.

Note that the "left" samples of sites 51b and 58, which showed abnormal absorption and fluorescence spectra compared to other samples, were supposed to be contaminated, and thereby these two samples were not used in the absorption and fluorescence analyses.

2.4 Soluble ions

The major soluble ions of surface snow water samples were analyzed with an ion chromatograph (Dionex, Sunnyvale, CA, USA) using an AS11 column for the anions SO_4^{2-}, NO_3^-, Cl^-, and F^- and a CS12 column for the cations Na^+, K^+, Ca^{2+}, Mg^{2+}, and NH_4^+. The soluble ions showed no obvious differences between filtered and unfiltered samples (Pu et al., 2017). According to Pio et al. (2007), the K^+ can be separated into three fractions: sea salt (ss), dust and others (the fraction not related to sea salt and mineral dust, nss-ndust). The nss-ndust-K^+ is a good maker for biomass burning (Pio et al., 2007). The Ca^{2+}concentrations of our samples were mostly larger than that of Na^+, leading to much larger mass ratios of Ca^{2+}/Na^+ than that in sea water (0.038) (Pio et al., 2007). Therefore, Ca^{2+} is dominated by the dust fraction and not corrected to nss-Ca^{2+} in this study. nss-ndust-K^+ is calculated using the following formulas (Pio et al., 2007):

$$\text{nss-ndust-}K^+ = K^+ - \text{ss-}K^+ - \text{dust-}K^+, \quad (7)$$

$$\text{ss-}K^+ = 0.038 \times \text{ss-}Na^+, \quad (8)$$

$$\text{ss-}Na^+ = Na^+ - 0.14 \times Ca^{2+}, \quad (9)$$

$$\text{dust-}K^+ = 0.028 \times Ca^{2+}. \quad (10)$$

In Eq. (8), 0.038 is the mass ratio of K^+/Na^+ in the sea water (Pio et al., 2007). In Eq. (9), the lowest mass ratio of Na^+/Ca^{2+} of our samples (0.14) is used to evaluate the dust fraction of Na^+. Similarly, the lowest mass ratio of K^+/Ca^{2+} (0.028) is used in Eq. (10) to calculate the dust fraction of K^+.

2.5 Hierarchical cluster analysis

A hierarchical cluster analysis was used to classify the samples based on the relative abundances of three PARAFAC components. Euclidean distance was used to estimate the distances between samples. Before determining the clustering method, the cophenetic correlation coefficients for the cluster trees created by different methods were calculated, including unweighted average, weighted average, centroid, farthest neighbor, shortest neighbor, weighted center of mass and Ward's methods. Finally, the unweighted average method was chosen due to the highest correlation coefficients. A total of four clusters were determined and labeled as clusters A-D.

2.6 Air mass backward trajectories and active fire data

Air mass backward trajectory has been widely used to identify the sources of air pollution (Stein et al., 2015), and also successfully applied to the studies of impurities in snow (Hegg et al., 2010; Wang et al., 2015; Zhang et al., 2013). In this study, 72-h air mass backward trajectories were conducted by the HYbrid Single-Particle Lagrangian Integrated Trajectory (HYSPLIT) model (version 4, http://ready.arl.noaa.gov/HYSPLIT.php). The model was run at 500 m above ground level four times a day for a period of 30 days preceding the sampling date at a given site. Combined with the satellite fire location map, the backward trajectories pass through the fires can be identified as the sources of biomass burning particles to the receptor sites (Antony et al., 2014; Hegg et al., 2010; Zhang et al., 2013). We used the active fire data from the Moderate Resolution Imaging Spectroradiometer (MODIS) Collection 6 (MCD14DL) and the Visible Infrared Imaging Radiometer Suite (VIIRS)

(VNP14IMGTDL_NRT) to capture potential fire location distributions. The data are available online: http://earthdata.nasa.gov/firms.

3 Results and discussion

3.1 The absorption characteristics of CDOM (a_{280}, $S_{275-295}$ and AAE)

The distributions of a_{280} and $S_{275-295}$ are shown in Fig. 3, and the corresponding values are summarized in Table 1. a_{280} ranged widely from 0.15 to 10.57 m^{-1} with an average of 1.69±1.80 m^{-1}. The highest value appeared at site 67 (10.57 m^{-1}), followed by sites 53, 79 and 47 (5.25 m^{-1}, 3.13 m^{-1} and 3.11 m^{-1}, respectively). Most of these samples were collected from the snow drifts. These values were higher than the a_{280} of snow, ice and cryoconite CDOM on the Tibetan Plateau (typically lower than 2.0 m^{-1}) (Feng et al., 2016, 2017). The lowest value was found at site 66 (0.15 m^{-1}), followed by sites 70, 82, 73, and 83 (0.21 m^{-1}, 0.23 m^{-1}, 0.30 m^{-1}, and 0.31 m^{-1}, respectively), and these values were compared to the absorption of soluble light-absorbing species in Alaskan snow with typical values of 0.1-0.15 m^{-1} at 250 nm (Beine et al., 2011). Some of these samples comprised freshly fallen snow and some were collected at remote sites that were far from pollution sources (Pu et al., 2017). The values of $S_{275-295}$ ranged from 0.0129 to 0.0389 nm^{-1} with an average of 0.0243±0.0073 nm^{-1}. $S_{275-295}$ is never reported in the terrestrial snow and ice samples before, but is widely measured in the aquatic environments. For example, Hansen et al. (2016) summarized the $S_{275-295}$ for oceanic and terrestrial systems, the values range of 0.020-0.030 nm^{-1} for ocean, 0.010-0.020 nm^{-1} for coastal water, and 0.012-0.023 nm^{-1} for terrestrial systems. The $S_{275-295}$

in this study covered the typical values in different types of natural water bodies, indicating complex compositions and sources of CDOM in seasonal snow across northwestern China. The AAEs of 19 CDOM samples are also shown in Table 1, which ranged from 4.41–8.91 with an average of 5.55±1.11. This value is comparable with the average AAE of HULIS extracted from Alaskan snow (6.11, from 300 to 550 nm) (Voisin et al., 2012).

The detailed results of each region are discussed below. Region 1 (sites 47-52) is located in the eastern Tibetan Plateau, which is typically higher than 4000 m above sea level. In this region, the snowpack was usually patchy and thin (Fig. 2a). During windy time, local soil can be blown and deposited on the snow surface, which had been observed by previous studies (Pu et al., 2017; Ye et al., 2012). Moreover, the filters for samples in this region were in yellow color due to high loading of soil dust. The average a_{280} was highest among all five regions (2.30±0.52 m^{-1}), and the $S_{275-295}$ fell in the range of 0.0170–0.0212 nm^{-1} (0.0188±0.0015 nm^{-1} on average), which shows the similar values of leaching for permafrost on the Tibetan Plateau (Wang et al., 2018).

In region 2 (sites 53-59, 61, and 79), snow at some sites was patchy (e.g., sites 53, 57, 61 and 79, Fig. 2b) and some sites were farmland (e.g., sites 55 and 56, Fig. 2c), which all can be influenced by local soil due to strong wind or agriculture activities. The a_{280} values of these sites were in the range of 1.66-5.25 m^{-1}. Several sites in this region showed lower a_{280} (0.41-0.54 m^{-1}, e.g., sites 54, 58 and 59), might resulting from new fallen snow or long distances from human activities (high altitude). Overall, region 2 showed a high average a_{280} (2.00±1.50 m^{-1}), and the average $S_{275-295}$ was

0.0229±0.0073 nm^{-1}.

Region 3 (sites 60, 62, 63 and 80-84) is the most developed part of Xinjiang, and major industrial cities are located here (e.g., Urumqi, Shihezi, Kuytun and Karamay). Therefore, human activities may dominate the contribution of CDOM in snow in this region. However, the a_{280} values were mostly less than 1.0 m^{-1} except at sites 60 and 84, and the average value was low (0.93±0.68 m^{-1}). Because samples of these sites were almost new fallen snow, the deposition of pollutants to the snowpack can be quite slight. Sites 60 and 84 were both close to industrial cities (Fig. 1 in Pu et al. (2017)), and the locally anthropogenic pollutants may be responsible for the high a_{280} (2.39 m^{-1} and 1.65 m^{-1}, respectively). The average $S_{275-295}$ was 0.0218±0.0057 nm^{-1} in this region.

In region 4 (sites 64-71), the maximal and minimal a_{280} values of the entire campaign, 10.57 m^{-1} (site 67, snow drift, Fig. 2d) and 0.15 m^{-1} (site 66, new snow), were found here. Generally, the a_{280} was in the range of 0.5-2.0 m^{-1} with an average of 0.80±0.62 m^{-1} (excluded site 67), which was the lowest compared to the values in the other regions. The mean value of $S_{275-295}$ (0.0255±0.0060 nm^{-1}) was higher than that in regions 1-3.

In region 5 (sites 72-78), the average value of a_{280} was 1.17±0.63 m^{-1}, which was intermediate among five regions. The $S_{275-295}$ was typically higher than 0.0300 nm^{-1} with an average of 0.0324±0.0060 nm^{-1}. This value was highest among five regions.

3.2 The fluorescence characteristics of CDOM

3.2.1 PARAFAC components

The EEMs of snow samples were analyzed by PARAFAC model, and three fluorescent components (C1-C3) were identified (Fig. 4). The corresponding excitation and emission loading spectra of each component is shown in the Supplement as Fig. S2. The excitation/emission (Ex/Em) wavelengths of each component's fluorescence peaks are summarized in Table 2.

C1 showed a primary peak at <240/453 nm for Ex/Em, which was similar to the component 1 reported by Stedmon and Markager (2005b) (Ex/Em = <250/448). This kind of fluorophore absorbs light mainly in the UVC band and shows a broad emission peak, which is usually identified as terrestrial FDOM (Stedmon et al., 2003). The appearance of a secondary peak at longer excitation wavelength (Ex/Em = 305/453 nm) may indicate that C1 is more aromatic and has higher molecular weight (Coble et al., 1998). C1 also resembled another terrestrial fluorophore, namely, component 4 in Stedmon and Markager (2005b) (Ex/Em = <250(360)/440), which has been widely found in nature fresh water environments and even water-extracted organic matter in aerosols (Chen et al., 2016; Mladenov et al., 2011; Zhang et al., 2009; Zhao et al., 2016).

C2 had a primary (secondary) peak at <240(300)/393 nm (Ex/Em), which was first measured in the oceanic system by Coble (1996). Subsequently, Stedmon et al. (2003) found a similar fluorophore (component 4 therein) in a terrestrially dominated estuary region. The following studies suggested that the C2-like component is also linked to microbial activity and phytoplankton degradation in natural aquatic systems (Yamashita et al., 2008; Zhang et al., 2009) or DOM in wastewater from anthropogenic sources (Stedmon and Markager, 2005b).

C3 is a typical fluorophore that is categorized as tyrosine-like FDOM and that exhibits Ex/Em pairs of <240(270)/315 nm. C3 reflects autochthonously labile DOM produced by biological processes (Stedmon et al., 2003) and has been commonly reported in previous studies of natural water bodies and the water extraction of aerosols (Chen et al., 2016; Murphy et al., 2008; Stedmon and Markager, 2005a).

3.2.2 Regional variation in PARAFAC components

Figure 5 shows the variations of three fluorescent components among regions, including the intensities and the relative contributions. Overall, C2 was the most intense fluorophore and accounted for 42% on average of the total fluorescence intensity of all samples, followed by C3 (38% on average) and C1 (20% on average). Compared to glacial snow and ice samples, which were dominated by protein-like substances (Dubnick et al., 2010; Feng et al., 2016), the seasonal snow samples in this study showed fewer microbial characteristics. According to Thieme et al. (2016), although we might underestimate the %C1 (approximately -3%) and overestimate the %C2 (approximately +6%) due to the preservation artifacts, it only slightly changes the results showed here.

In Qinghai (region 1), the most obvious feature was that C1 accounted for approximately 35% of the total fluorescence intensity on average. This value was significantly higher than the other regions. In contrast, %C3 in region 1 was quite low (24% on average). This result was mainly due to the high F_{max}(C1) in region 1 since the regional variation of F_{max}(C3) was slight (Fig. 5).

In Xinjiang (regions 2-5), %C1 varied by region, while %C2 and %C3 were roughly equal. In region 2, %C1 was also high (25% on average). However, %C1 showed the lowest value (9% on average) in region 3, where most of the samples were new fallen snow (7 of 8 sites). The great difference between %C1 and %C2 in this region indicated different sources of these two humic-like components. In regions 4 and 5, %C1 were nearly double of that in region 3 (both were approximately 17%).

At sites 54 and 82, the relative abundance of C3 exceeded 70%. This value was approximately twofold higher than the average of the whole dataset (38%). This result can be explained by two possible reasons, (1) lower inputs of C1 and C2, and (2) greater biological activities were available in the snowpack at these sites. We found lichens near these two sites (Fig. S3), providing evidence for the latter reason.

At site 67, the fluorescence intensities were highest among all samples (0.30 RU, 0.39 RU, and 0.38 RU for C1, C2, and C3, respectively), especially for C3. The average F_{max}(C3) was 0.10 RU (excluded site 67), with a low standard deviation of 0.02 RU, and this value was approximately one-fourth of that at site 67. Therefore, rather than owing to microbial activity alone, the extremely high F_{max}(C3) of site 67 may be due to other sources, for instance, some organic compounds released from diesel combustion may show similar spectra (Mladenov et al., 2011).

To assess the similarities and differences between samples, a hierarchical cluster analysis based on the relative intensities of fluorescent components was conducted (Fig. 6). The snow samples were separated into four clusters (clusters A-D) (Fig. S4). Samples classified into clusters A and B were dominant. The high %C1, which was 34%

on average, was the most remarkable feature of cluster A and led to a low %C3 (26% on average). All samples in region 1 and most samples in region 2 were assigned to cluster A. For cluster B, %C1 was low (13% on average), and %C3 (47% on average) was slightly higher than %C2 (40% on average). For sites in northern Xinjiang (regions 4 and 5), most samples were classified into cluster B. The samples assigned to cluster C, including those of sites 60, 62, 69, 72, 76 and 84, showed dominant contributions of C2 (57% on average). Half of these samples were found in region 3, and the others were dispersed in regions 4 and 5. Cluster D contained only two samples from sites 54 and 82. The difference between cluster D and the others was an extremely high contribution of protein-like component C3 (73% on average), which indicated the high bioavailability of snow CDOM.

3.2.3 Fluorescence-derived indices

The regional variations of three established fluorescence-derived indices are shown in Fig. 7 and the values of each site are in Table 1. The HIX of samples in this study fell into the range of 0.16-3.20 with an average of 1.21±0.78. The highest average HIX appeared in region 1 (2.21±0.42), demonstrating high degree of humification of snow CDOM. The lowest average HIX was found in region 3 (0.62±0.37 on average), which suggests that the CDOM was fresh. This finding is easily explained by the fact that nearly all of snow samples in this region were new fallen snow. Compared to the HIX of other types of samples (Table 3), the HIX of snow across northwestern China was higher than that of spring water (Birdwell and Engel, 2010); comparable to cryoconite

in glaciers from the Tibetan Plateau (Feng et al., 2016), inland lakes (Zhang et al., 2010) and north Pacific Ocean water (Helms et al., 2013); and was lower than cave water (Birdwell and Engel, 2010), estuarine water (Huguet et al., 2009), fog water (Birdwell and Valsaraj, 2010), groundwater (Huang et al., 2015), water extraction of alpine aerosol (Xie et al., 2016) and urban aerosol (Mladenov et al., 2011).

According to McKnight et al. (2001) and Huguet et al. (2009), the values of FI > 1.9 or BIX > 1.0 indicate microbially derived DOM. The BIX and FI for the snow samples were typically below 1.0 and 1.9, respectively, implying unremarkably autochthonous characteristics. The regional distributions of BIX and FI corresponded with that of HIX. The samples with highest average BIX and FI were in region 3 (0.93±0.25 and 1.60±0.15, respectively), and the samples in region 1 exhibited the lowest average values (0.49±0.05 and 1.29±0.05, respectively). The BIX and FI of different types of samples changed little, and the only exception was the FI of cryoconite in glaciers from the Tibetan Plateau (Feng et al., 2016), which was approximately twice as high as those of the other samples.

3.3 Source attribution of CDOM

3.3.1 Source identification of PARAFAC components

In Qinghai, As mentioned in Sec. 3.1, the snow packs were strongly influenced by the local soil dust, which was confirmed by the lowest average $S_{275\text{-}295}$, leading to a high %C1 (35% on average). This result implied that the terrestrial fluorophore C1 was mainly from the soil HULIS, and confirmed the invariably terrestrial source of the C1-

like fluorophores, regardless of whether in the natural water bodies, aerosol water extraction or snow.

Correlation analyses were conducted to assess the potential sources of C2. The mutual relationships between PARAFAC components were shown in Fig. 8. The F_{max}(C3) of site 67 were much higher than those of any other sample (shown as red markers in Fig. 8), which can strongly influence the results of the correlation analysis. When excluding the data of site 67, the R^2 between F_{max}(C1) and F_{max}(C3) fell from 0.316 to 0.082, and the linear relationship became nonsignificant (Fig. 8b). Therefore, we used the dataset that excludes site 67 in the analysis, and the results are shown below. F_{max}(C1) and F_{max}(C2) exhibited a significant and positive correlation (R^2 = 0.332, $p<0.001$); however, this value was much lower than those in previous studies of natural water, for instance, R^2 = 0.63 for inland lakes (Zhao et al., 2016) and R^2 = 0.88 for inland rivers (Zhang et al., 2011). This result indicated that soil dust only partly accounted for the source of C2. Meanwhile, a significant linear relationship (R^2 = 0.364, $p<0.001$) was found between F_{max}(C2) and F_{max}(C3), which implied a potential microbial source for C2, consistent with the finding of Yamashita et al. (2008). Not surprisingly, F_{max}(C1) and F_{max}(C3) showed no correlation (R^2 = 0.082, $p>0.05$). Furthermore, the correlation coefficients between F_{max} and three major ions were calculated. The results are shown in Table 4. F_{max}(C2) showed significant and positive correlations with three ions ($p<0.001$). The secondary ions SO_4^{2-} and NO_3^- are commonly considered as the markers of anthropogenic emissions from the burning of fossil fuel, such as oil and coal (Doherty et al., 2014; Oh et al., 2011; Pu et al., 2017),

and nss-ndust-K^+ is a good tracer of biomass burning (Pio et al., 2007). Therefore, C2 may also originate from anthropogenic pollution and biomass burning. Overall, there are four potential sources of snow CDOM in our study, since the contribution of microbial-derived C3 to a_{280} was low compared to C1 and C2 (Fig. S5), three major sources were identified, i.e., soil dust, biomass burning and anthropogenic pollution.

The ratios of intensities for PARAFAC components can be a useful tool to trace the CDOM sources (Murphy et al., 2008). In this study, the ratio of F_{max}(C2) and F_{max}(C1) was applied to assess the relative contributions of soil and non-soil (biomass burning and anthropogenic pollution) sources for snow CDOM (Fig. 9a). An analysis of variations (ANOVA) was used to test the differences among regions. Regions 1 and 2 showed low ratios of F_{max}(C2) and F_{max}(C1) (1.20±0.14 and 1.76±0.82 on average, respectively), indicating the strong influence from local soil dust. The values of F_{max}(C2)/F_{max}(C1) for regions 3, 4 and 5 were significantly higher (ANOVA, $p<0.05$) with averages of 5.57±2.26, 3.17±1.47 and 3.02±1.22, respectively. This result implies that the snow CDOM in these regions were different from those in regions 1 and 2, and mainly from the non-soil sources.

3.3.2 Regional variations

The regional variations of CDOM sources are discussed below using analyses of absorption and fluorescence characteristics, chemical species, and air mass backward trajectories. In addition, the sources of CDOM in snow are also compared with those of particulate light absorption of ILAPs.

In Qinghai (region 1), the lowest regional average and slight variation of $S_{275-295}$ indicated the dominant contribution of terrestrial sources for snow CDOM (e.g., local soil dust) (Fichot and Benner, 2012; Helms et al., 2008). This result is also verified by the fluorescence properties (highest HIX and %C1, lowest $F_{max}(C2)/F_{max}(C1)$). Although some of trajectories to site 47 passed through the active fires (Fig. 10a), compared to the strongly local soil input, the influence of long-range transportation of biomass burning aerosol was much fewer. Combined with the low value of $(SO_4^{2-}+NO_3^-)$/nss-ndust-K^+ (Fig. 9b), the CDOM produced by anthropogenic pollution is negligible in region 1. Above all, the soil dust is clearly the primary source of CDOM.

In region 2, the high relative intensities of C1 and low values of $F_{max}(C2)/F_{max}(C1)$ indicated that the contribution of soil to snow CDOM was also remarkable. Along the paths of the air masses to site 55 (Fig. 10b), very few trajectories encountered the fires. Additionally, the average of $(SO_4^{2-}+NO_3^-)$/nss-ndust-K^+ was also low, which showed an insignificant role of anthropogenic pollution. Therefore, in region 2, a major source of soil is reasonable.

In region 3, the extremely high averages of $F_{max}(C2)/F_{max}(C1)$ and $(SO_4^{2-}+NO_3^-)$/nss-ndust-K^+, which were significantly higher than those in other regions (ANOVA, $p<0.05$), implied a strong influence of anthropogenic pollution. The mass ratio of Cl^- and Na^+ (2.48, Fig. S6) was approximately 2 times higher than that in sea water (1.18, Hara et al., 2004), which indicated that Cl^- might originate from other sources in addition to sea salt, such as coal combustion (H. L. Wang et al., 2008; Y. Wang et al., 2006), while the values in other regions were comparable to 1.18. This

result, again, confirmed that the CDOM from pollution was dominant in region 3 but inapparent in other regions. The backward trajectories also showed consistent results (Fig. 10c). Most of the trajectories to site 84 came from the northwest and passed through the cities with heavy industry (e.g., Karamay and Shihezi). Therefore, the air pollutants can be transported to the sample area and deposited on the surface snow.

In regions 4 and 5, the non-soil sources of snow CDOM were predominant due to the high regional averages of $F_{max}(C2)/F_{max}(C1)$. In region 4, many of air masses, which originated from the central Asia (west), Siberia (north) and central Xinjiang (south), passed through the active fires, and strongly influenced this region (Fig. 10d). The ratios of $(SO_4^{2-}+NO_3^-)$ and nss-ndust-K^+ were significantly lower than those in region 3 (ANOVA, $p<0.05$), indicating a major source of biomass burning. Coincidentally, in region 5, the value of $(SO_4^{2-}+NO_3^-)$/nss-ndust-K^+ was comparable, which suggested CDOM from biomass burning rather than pollution. The respectable amount of air mass encountered the fires (Fig. 10e) can explain this finding. Furthermore, the low mass ratios of Cl^- and Na^+ in region 4 and 5 also implied the slight influence of anthropogenic pollution. Overall, biomass burning is the dominant source both in regions 4 and 5.

Pu et al. (2017) used a positive matrix factorization (PMF) model to identified the sources of particulate light absorption of ILAPs (denoted as C_{BC}^{max}) in snow during the same field campaign. The comparison of C_{BC}^{max} and a_{280} among regions is shown in Fig. S7. In regions 1, 2, and 5, there were no significant correlation between C_{BC}^{max} and a_{280}, which indicated the entirely different sources of CDOM and particulate absorption of ILAPs. As reported by Pu et al. (2017), the major sources of C_{BC}^{max} were biomass

burning in regions 1-2 and industrial pollution in region 5; while those of CDOM in this study were soil dust and biomass burning, respectively. Robust linear correlations were found in regions 3 and 4 (R^2 = 0.95 and 0.75, respectively), which implied high consistency for sources of CDOM and particulate absorption of ILAPs (i.e., anthropogenic pollution and biomass burning, respectively).

3.4 Comparing the light absorption by CDOM and BC

Figure 11 shows the relative contributions of CDOM and BC to light absorption. As mentioned above, light absorption within visible wavelengths was available for 19 samples. The BC concentrations in surface snow were obtained from Pu et al. (2017), and the MAC at 550 nm and the AAE of BC used in the calculation were 6.3 m^2 g^{-1} and 1.1, respectively (Pu et al., 2017).

The light absorption of CDOM was 0.02-1.17 (0.34±0.34 on average) times of that for BC at 400 nm. At 500 nm, this value decreased quickly to 0.10±0.11 on average and ranged from 0.01-0.40. This finding is quite different from the results for Alaskan snow. Dang and Hegg (2014) converted the CDOM absorption in snow at Barrow, Alaska, into equivalent BC mixing ratios of 0.14 ng g^{-1} at 400 nm and 0.07 ng g^{-1} at 550 nm. As presented by Doherty et al. (2013), the mixing ratio of BC in Barrow snow ranged from 10-30 ng g^{-1}. Hence, the absorption of CDOM in Alaskan snow can be safely ignored, but this does not appear reasonable for some areas across northwestern China.

Previous studies on impurities in seasonal snow have focused on insoluble particles

(e.g., BC, ISOC and dust) (Doherty et al., 2010, 2014; Pu et al., 2017; Wang et al., 2013). The above discussion indicates that in some specific areas of northwestern China, the absorption of CDOM in snow was remarkable. What is the common feature of such sites? Most of them were classified into cluster A (16 of 19 sites). The average $S_{275\text{-}295}$ (0.0187±0.0022) of these 19 sites was the lowest compared to the averages of regions 1-5. The averages of BIX (0.60±0.20), FI (1.31±0.09) and $F_{max}(C2)/F_{max}(C1)$ (1.66±1.03) were lower than those of region 2, in which the influence of local soil was obvious. Besides, the averages of HIX (1.87±0.57) and %C1 (30%) were higher than those of region 2. These results indicated that the CDOM of these sites was undoubtedly from terrestrial origins (e.g., wind-blown soil dust). Hence, we suggest that the absorption by CDOM in the snowpack, which is heavily affected by soil, cannot be ignored.

4 Conclusions

Seasonal snow samples were collected across northwestern China from January to February 2012. The a_{280} and $S_{275\text{-}295}$ of snow CDOM ranged from 0.15-10.57 m^{-1} and 0.0129-0.0389 nm^{-1}, respectively. The average value of a_{280} (1.69±1.80 m^{-1}) was approximately 10 times higher than that in Alaska (Beine et al., 2011). Samples in Qinghai (region 1) exhibited the highest average a_{280} (2.30±0.52 m^{-1}) and lowest average $S_{275\text{-}295}$ (0.0188±0.0015 nm^{-1}) resulting from the strong influence of local soil dust. Low average a_{280} appeared in central Xinjiang (region 3, 0.93±0.68 m^{-1}), where almost all the samples were collected from new fallen snow, and northwestern Xinjiang (region 4, 0.80±0.62 m^{-1} when excluded site 67) which was far from industrial areas.

In the Tianshan Mountains (region 2) and northeastern Xinjiang (region 5), the average values of a_{280} were 2.00±1.50 m^{-1} and 1.17±0.63 m^{-1}, respectively. For all sites in Qinghai and some of the sites in Xinjiang (19 of 39 sites), the light absorption of CDOM cannot be neglected and even was remarkable (0.34±0.34 times relative to BC at 400 nm on average) due to the high contribution of soil dust to snow CDOM. Hence, we suggest that the CDOM absorption in the visible wavelengths at such sites should be taken into consideration in future studies.

Based on PARAFAC analysis, two humic-like fluorophores (C1 and C2) and one protein-like fluorophore (C3) were identified. In Qinghai (region 1), %C1 (35% on average) was much higher than those of the other regions, and the highest HIX, lowest BIX and FI were also found. In Xinjiang (regions 2-5), %C1 varied among regions. In region 2, C1 accounted for approximately 25% to the total fluorescence, followed by regions 4 and 5 (both were 17% on average). In region 3, the C1 contribution was lowest (9% on average), and the values of fluorescence-derived indices also showed the consistent results (the lowest HIX, highest BIX and FI). A hierarchical cluster analysis was used to classify samples into four clusters (A-D) based on the relative intensities of three fluorescent components. All samples in region 1 and most samples in region 2 were assigned to cluster A (a high contribution of C1). The number of samples assigned to cluster B (roughly equal contributions of C2 and C3) and cluster C (a dominant contribution of C2) were nearly even in region 3. For regions 4 and 5, most samples were classified into cluster B. Only two samples were assigned to cluster D due to the dominant contribution of C3.

According to the correlation analysis between F_{max}(C2) and three major ions (SO_4^{2-}, NO_3^-, and nss-ndust-K^+), as well as the mutual relationships among the fluorescent components, C2 exhibited potential sources of soil, microbial activity, anthropogenic pollution, and biomass burning. Furthermore, the regional distribution of CDOM sources was assessed by using variations of $(SO_4^{2-}+NO_3^-)$/nss-ndust-K^+, Cl^-/Na^+, F_{max}(C2)/F_{max}(C1) and air mass backward trajectory analysis. The major sources for the five regions were soil dust in regions 1-2, anthropogenic pollution in region 3, and biomass burning in regions 4-5.

This study investigated the optical characteristics and potential sources of CDOM in seasonal snow across northwestern China. Future studies should focus on the molecular characteristics of snow CDOM and its relationship with the optical properties, which is of great importance to the energy budget of snowpack and the global carbon cycle.

Data availability. All datasets and codes used to produce this study can be obtained by contacting Xin Wang (wxin@lzu.edu.cn). The elevation data used in this study are available at http://rda.ucar.edu/datasets/ds759.3/#!access.

Competing interests. The authors declare that they have no conflict of interest.

Acknowledgements. This research was supported by the Foundation for Innovative Research Groups of the National Natural Science Foundation of China (41521004), the National Natural Science Foundation of China (41522505 and 41775144), and the Fundamental Research Funds for the Central Universities (lzujbky-2018-k02). We thank Jinsen Shi of Lanzhou University, Hao Ye of Texas A&M University, and Rudong

Zhang of Nanjing University for their assistance in field sampling.

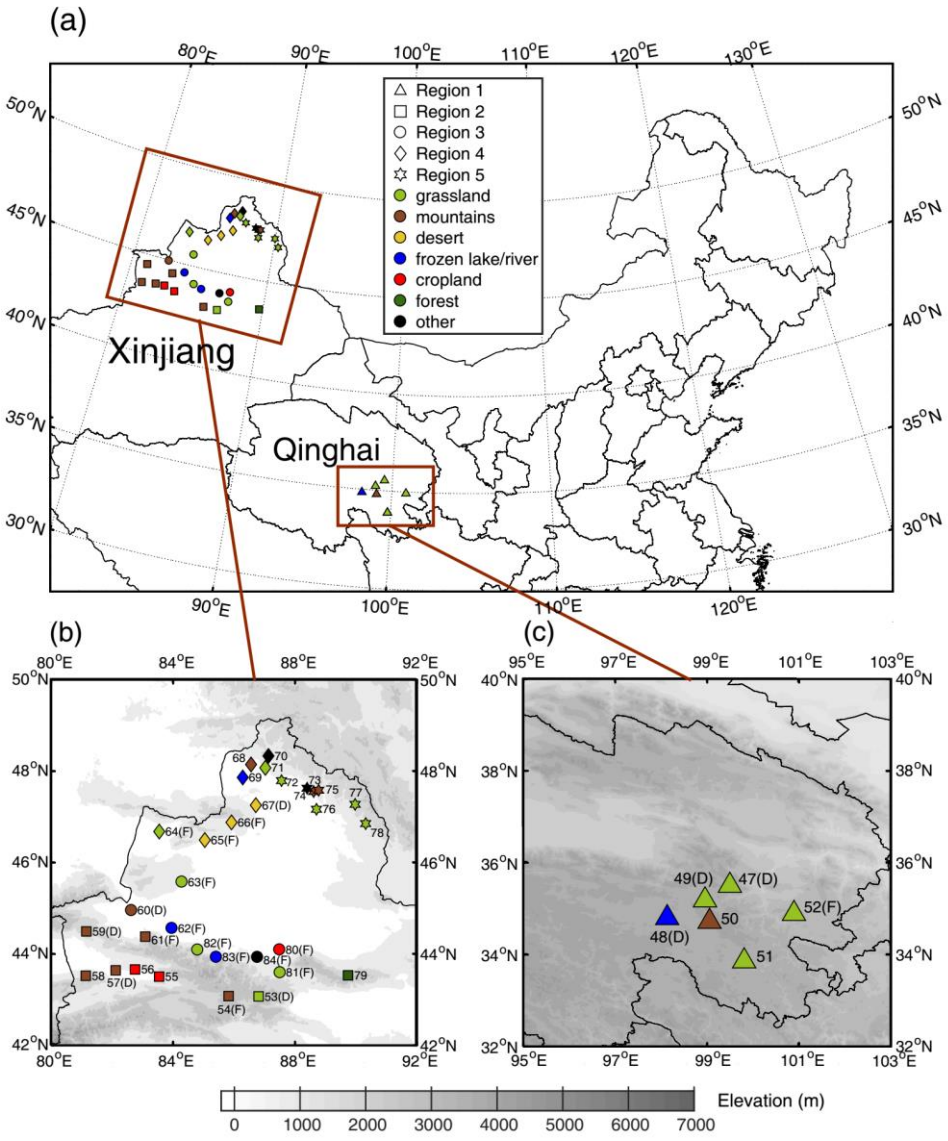

Figure 1. (a) The location of study area and sample site distribution across northwestern China. The site numbers and regional groupings are shown in panel (b) for Xinjiang and (c) for Qinghai. Sample areas are divided into five regions indicated by different symbol shapes, and the land cover types of sample sites are represented in different colors, as shown in the legend in panel (a). The "D" indicates that the sample was collected from a snow drift, and the "F" indicates that the surface sample was fresh snow. The elevation is shown in the contour plot.

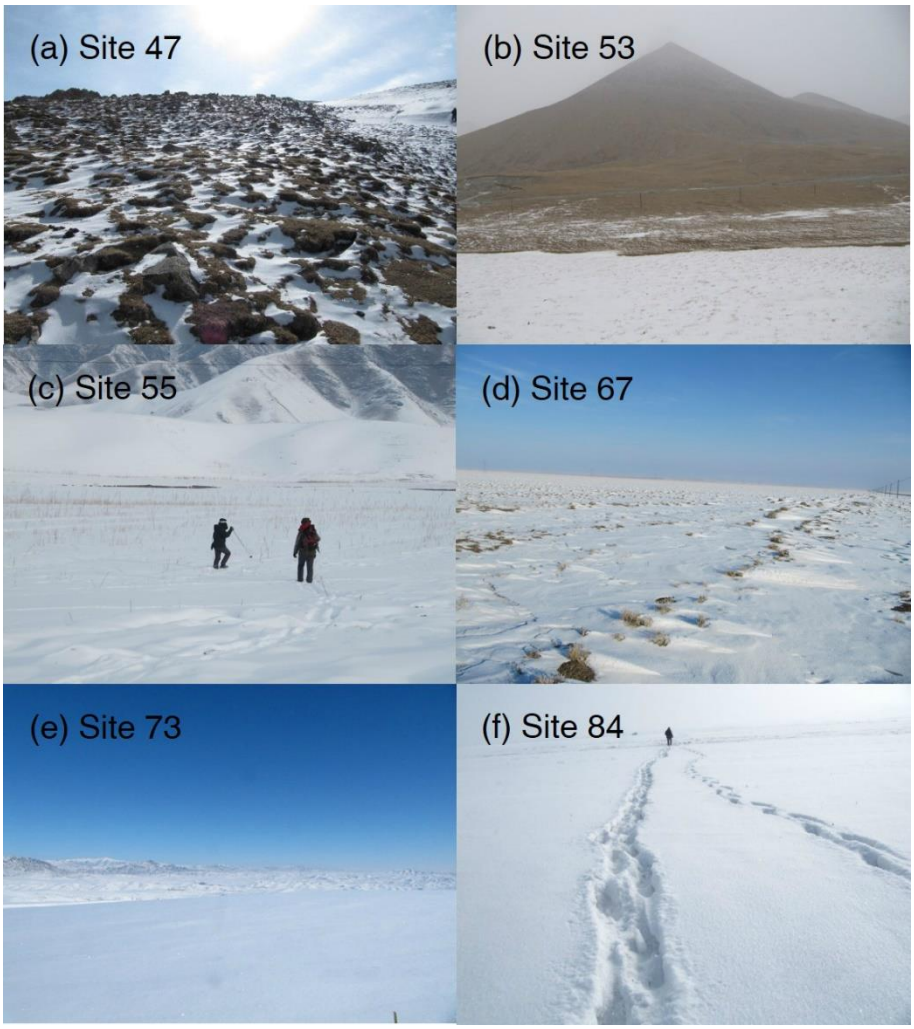

Figure 2. Pictures of typical sample sites.

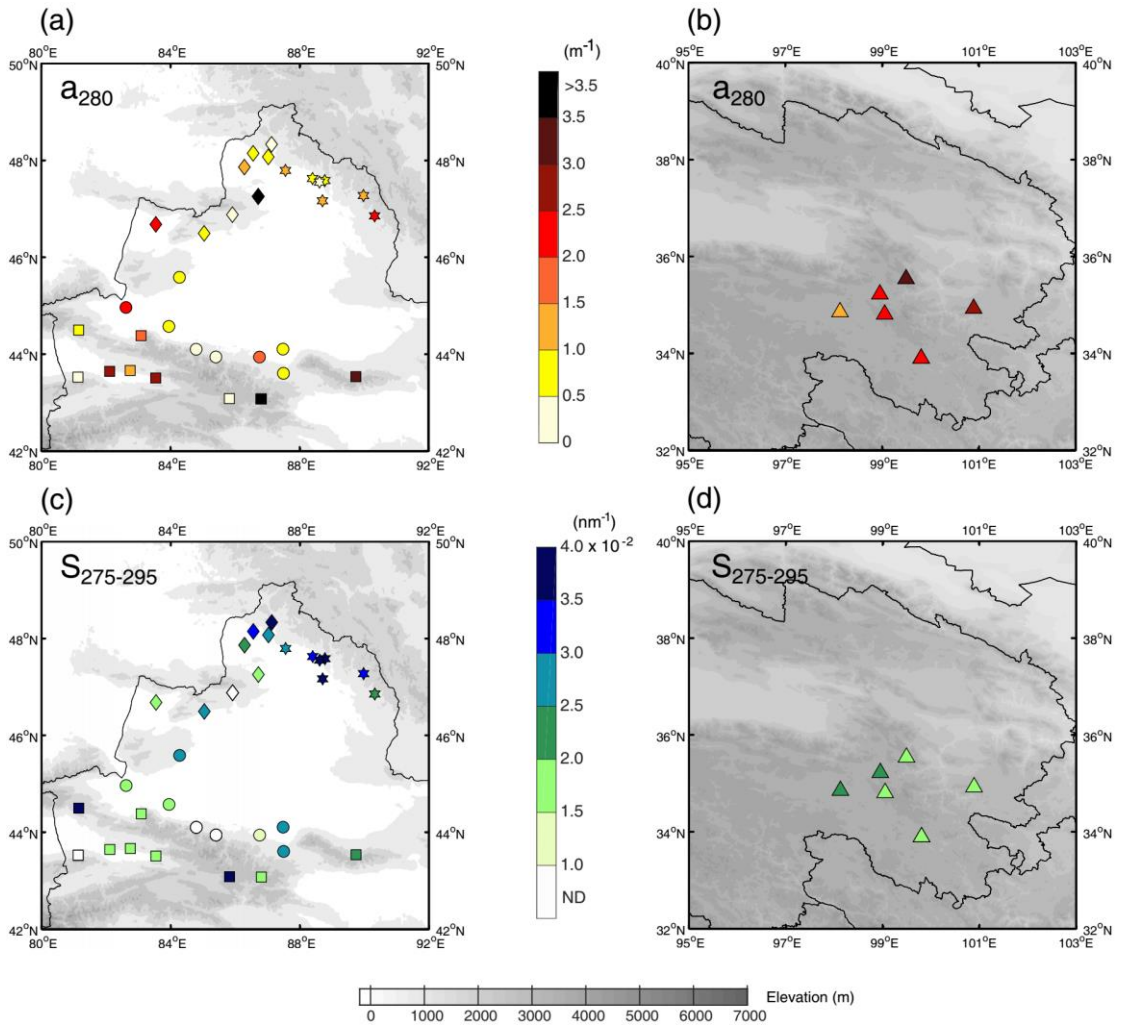

Figure 3. a_{280} and $S_{275\text{-}295}$ for sites in (a, c) Xinjiang and (b, d) Qinghai, respectively. The five regions are indicated by different symbols (same as Fig. 1).

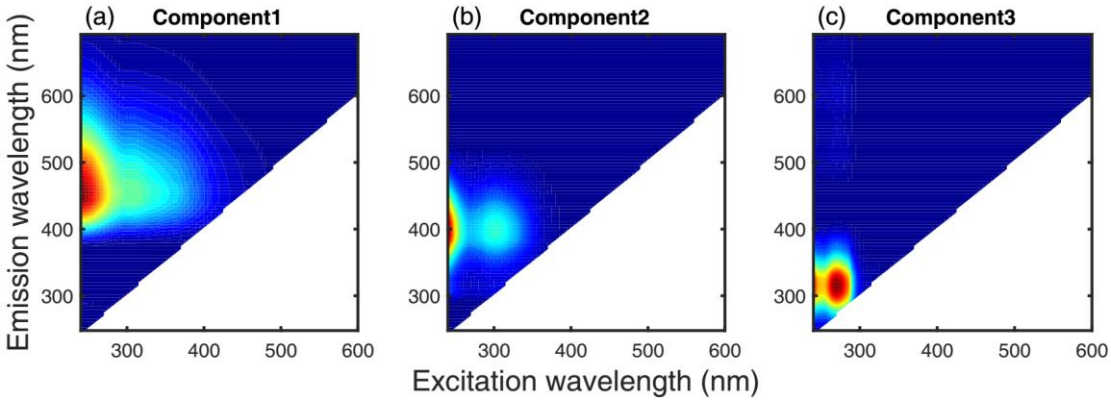

Figure 4. The fluorescent components identified by the PARAFAC analysis.

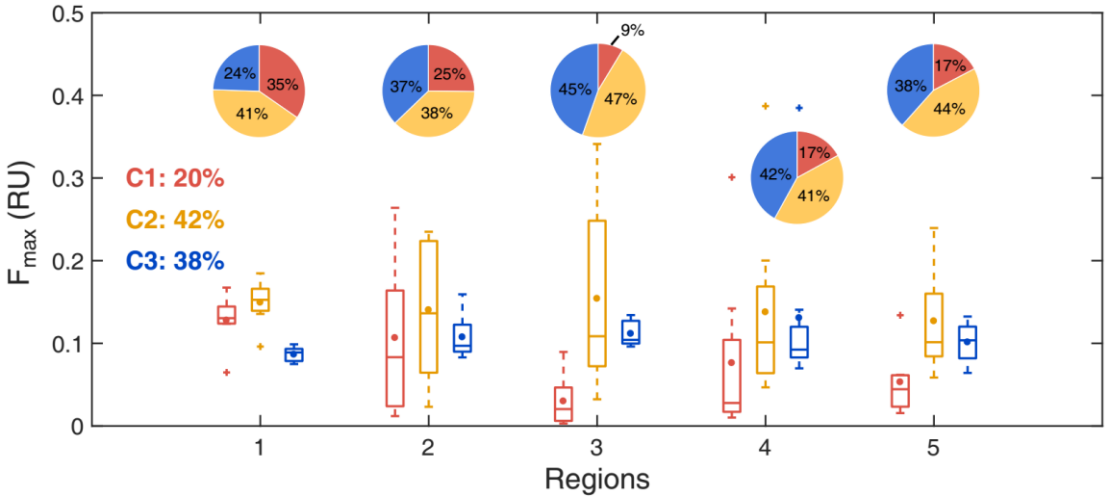

Figure 5. Variations of the fluorescent components among regions. The boxplots show the intensities of components. The boxes denote the 25th and 75th quantiles, and the horizontal lines represent the 50th quantiles (medians), the averages are shown as dots; the whiskers denote the maximum and minimum data within 1.5 times of interquartile rang, and the datapoints out of this range are marked as "+". The pie charts show the average relative contributions of three components in each region. C1, C2, and C3 are represented in red, yellow, and blue, respectively, both for the boxplots and pie charts. The percentages on the left of the panel are the averages of %C1-%C3 for the whole dataset.

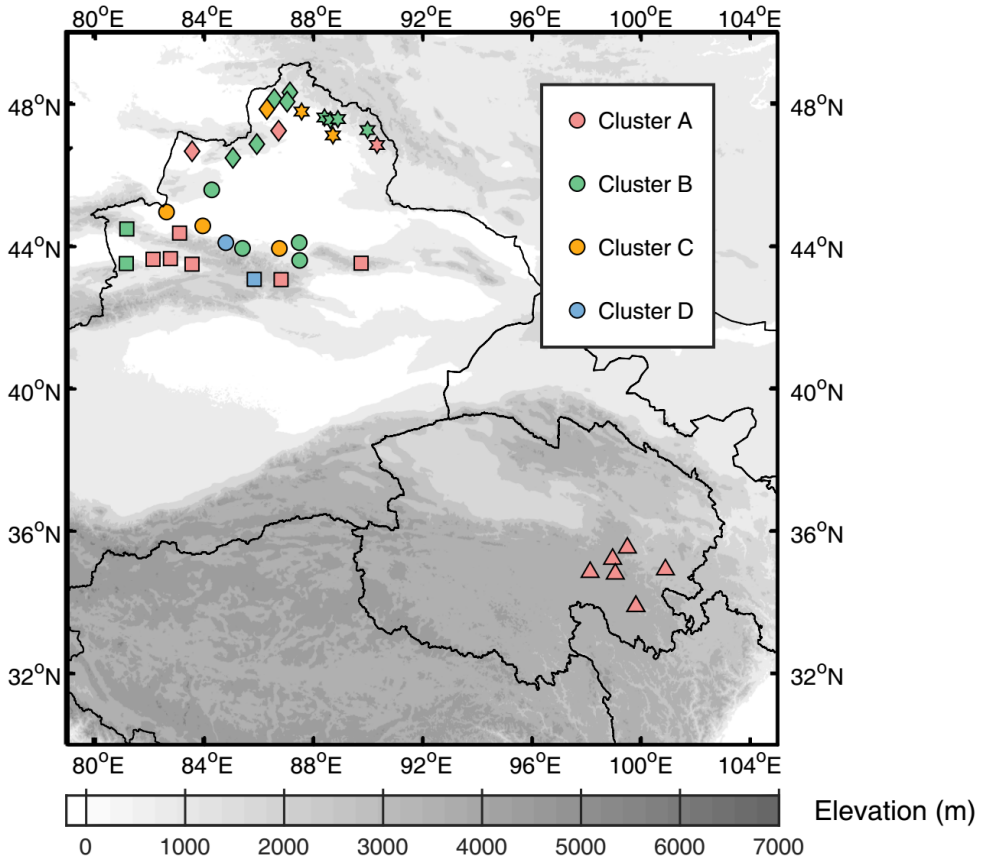

Figure 6. Hierarchical cluster analysis based on the relative intensities of fluorescent components.

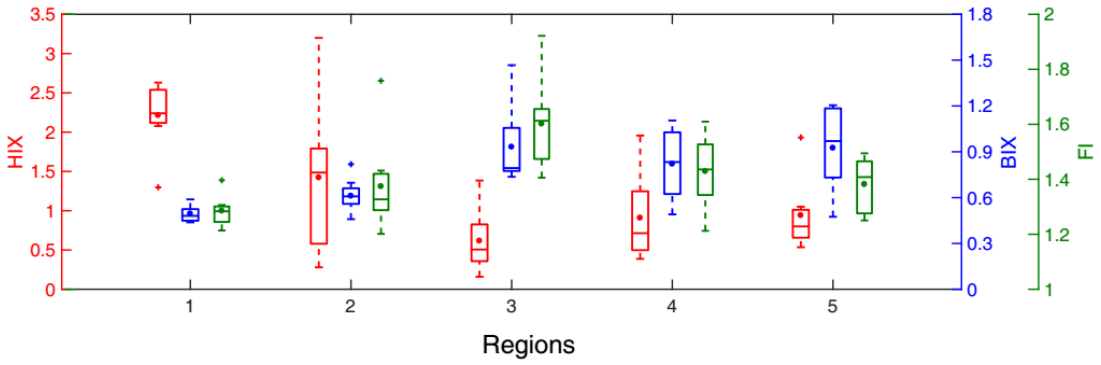

Figure 7. HIX (shown in red), BIX (shown in blue) and FI (shown in green) of surface snow samples among regions. The meaning of each part of box is same as that in Fig. 5.

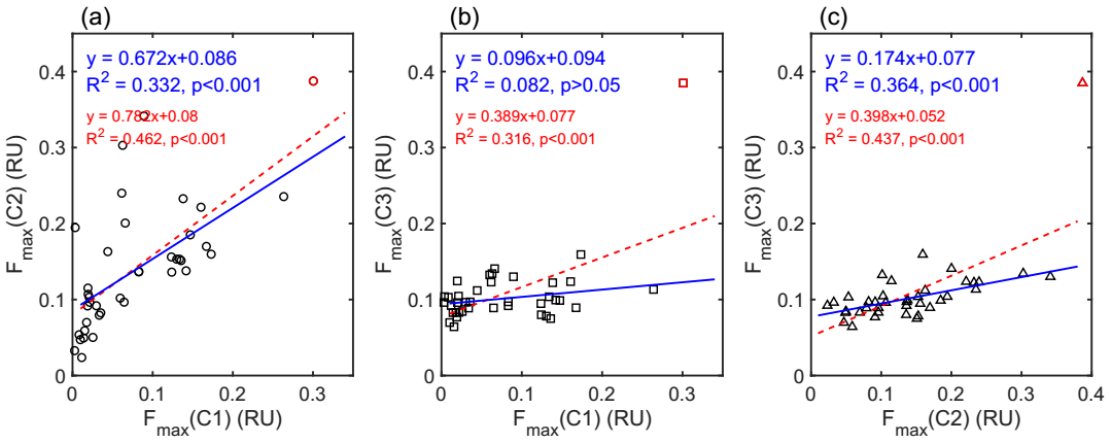

Figure 8. The linear relationships between intensities of (a) C1 and C2, (b) C1 and C3, (c) C2 and C3. The red dashed lines show the fit of the entire dataset, and the blue solid lines show the fit of data excluded site 67 (shown as markers in red). The corresponding fitting parameters are exhibited in the same color, including the equations, correlation coefficients and p-values.

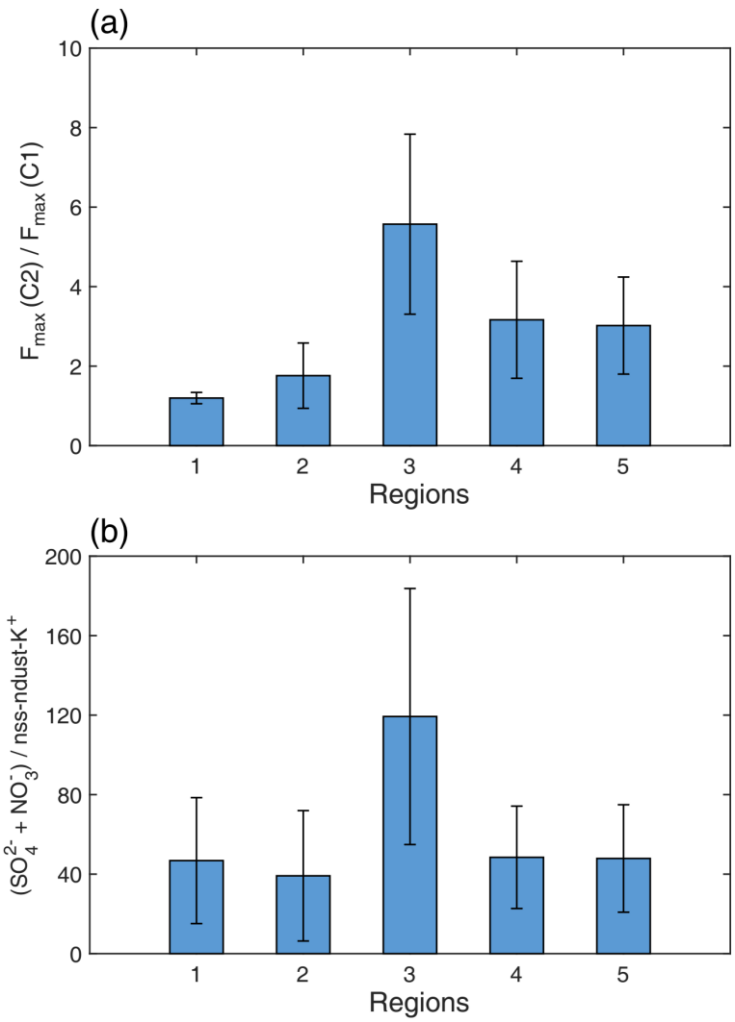

Figure 9. The regional averages of the ratios for (a) F_{max}(C2) and F_{max}(C1), (b) $(SO_4^{2-}+NO_3^-)$ and nss-ndust-K^+.

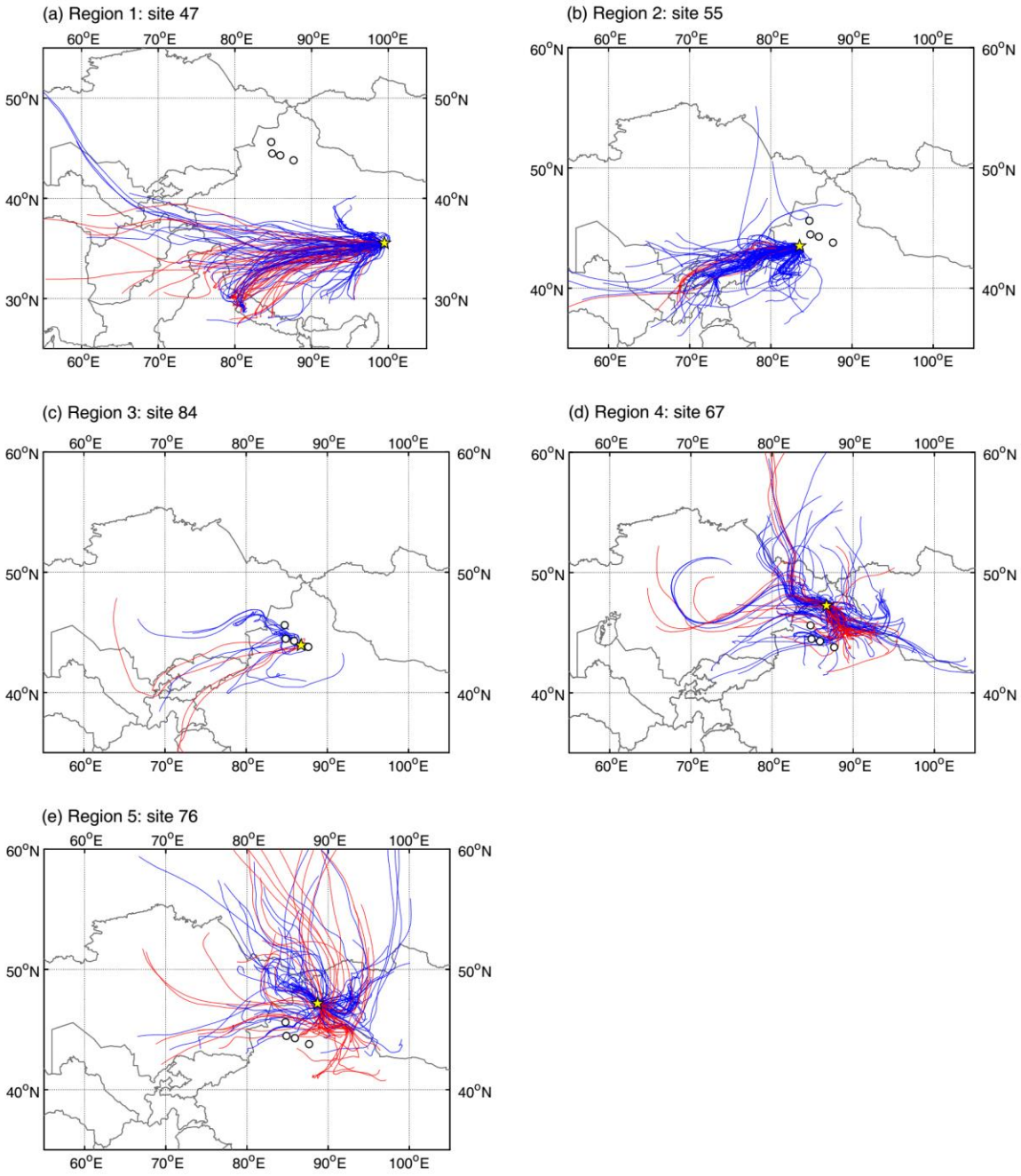

Figure 10. 72-h air mass backward trajectories at 500 m above ground level with the initial positions at representative sites (shown as yellow pentagrams) in each region. Trajectories were calculated four times per day for a period of 30 days preceding the sampling date at a given site by HYSPLIT (version 4, NOAA) except for panel (c). Since the snow was fresh at site 84, the trajectories were derived for 5 days preceding the sampling date. The red lines show the airmasses passed through the active fires

before reaching the receptor sites, and the blue lines are those did not pass the fires. The white dots represent the typical industrial cities in Xinjiang, i.e., Karamay, Kuytun, Shihezi and Urumqi from west to east.

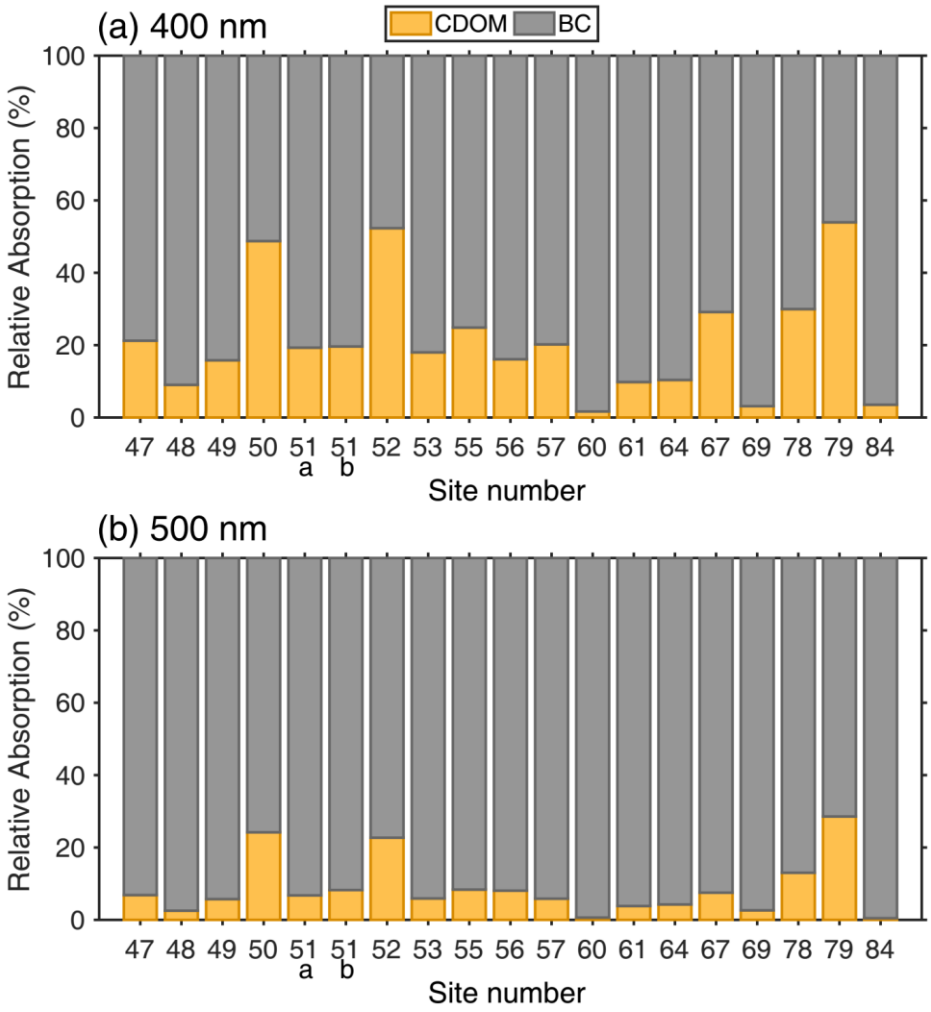

Figure 11. The relative absorption contributions of CDOM (yellow bar) and BC (gray bar) at **(a)** 400 nm and **(b)** 500 nm.

Table 1. Statistics on absorption and fluorescence parameters for surface snow at each site. Note: N. A. for no data.

Site	Lat. (N)	Lon. (E)	a_{280} (m^{-1})	$S_{275-295}$ (nm^{-1})	AAE	HIX	BIX	FI
47	35.54	99.49	3.11	0.0174	4.66	2.24	0.51	1.31
48	34.85	98.13	1.32	0.0212	5.12	1.30	0.59	1.40
49	35.22	98.95	2.14	0.0206	5.20	2.24	0.47	1.29
50	34.80	99.05	2.38	0.0194	4.91	2.08	0.48	1.27
51a	33.89	99.80	2.44	0.0183	4.87	2.44	0.44	1.21
51b	33.89	99.80	2.02	0.0175	4.91	2.57	0.44	1.28
52	34.92	100.89	2.71	0.0170	4.63	2.63	0.53	1.23
53	43.07	86.81	5.25	0.0178	4.53	3.20	0.48	1.25
54	43.08	85.82	0.41	0.0350	N.A.	0.28	0.82	1.76
55	43.51	83.54	2.52	0.0178	5.13	1.90	0.61	1.30
56	43.66	82.75	1.38	0.0192	5.77	1.39	0.61	1.31
57	43.64	82.11	2.66	0.0168	5.31	1.75	0.59	1.33
58	43.52	81.13	0.42	N.A.	N.A.	0.54	0.70	1.42
59	44.49	81.15	0.54	0.0357	N.A.	0.59	0.65	1.43
60	44.96	82.63	2.39	0.0174	8.91	1.38	1.24	1.43
61	44.38	83.09	1.66	0.0189	6.06	1.49	0.59	1.36
62	44.57	83.96	0.80	0.0194	N.A.	0.52	1.47	1.63
63	45.58	84.29	0.81	0.0264	N.A.	0.71	0.78	1.41
64	46.68	83.54	2.01	0.0194	5.54	1.96	0.49	1.21
65	46.49	85.04	0.64	0.0291	N.A.	0.77	0.82	1.39
66	46.88	85.92	0.15	N.A.	N.A.	0.39	0.84	1.61
67	47.26	86.71	10.57	0.0169	4.41	1.47	0.63	1.30
68	48.15	86.56	0.57	0.0301	N.A.	0.59	1.10	1.54
69	47.86	86.29	1.41	0.0221	7.70	1.02	1.04	1.48
70	48.33	87.13	0.21	0.0351	N.A.	0.41	0.62	1.39
71	48.07	87.03	0.61	0.0255	N.A.	0.66	1.01	1.52
72	47.79	87.56	1.49	0.0259	N.A.	1.05	1.20	1.41
73	47.55	88.61	0.30	0.0381	N.A.	0.54	1.12	1.45
74	47.63	88.40	0.55	0.0337	N.A.	0.63	1.20	1.49
75	47.58	88.78	0.81	0.0376	N.A.	0.74	0.79	1.34
76	47.17	88.70	1.21	0.0389	N.A.	0.89	0.97	1.47
77	47.27	89.97	1.50	0.0301	N.A.	0.80	0.71	1.25
78	46.85	90.32	2.32	0.0221	5.52	1.93	0.48	1.25
79	43.53	89.74	3.13	0.0221	5.52	1.65	0.46	1.20
80	44.10	87.49	0.54	0.0292	N.A.	0.49	0.74	1.66
81	43.60	87.51	0.72	0.0255	N.A.	0.45	0.80	1.65
82	44.09	84.80	0.23	N.A.	N.A.	0.16	0.88	1.92
83	43.93	85.41	0.31	N.A.	N.A.	0.27	0.77	1.60
84	43.93	86.76	1.65	0.0129	6.66	0.95	0.79	1.52

Table 2. Description of the three PARAFAC components. The secondary peaks are shown in brackets.

Component number	Excitation maximal wavelength (nm)	Emission maximal wavelength (nm)	Descriptions	References
C1	<240 (305)	453	Terrestrial humic-like substances	Stedmon and Markager, 2005b; Stedmon et al., 2003
C2	<240 (300)	393	Microbial, anthropogenic or terrestrial humic-like substances	Murphy et al., 2011; Zhang et al., 2010
C3	<240 (270)	315	Tyrosine-like fluorophore	Yu et al., 2015

Table 3. The fluorescence-derived indices in this study and summary of that from natural water and water extraction of aerosol reported by other studies with average values for some studies are shown in brackets.

Study area	Sample type	HIX	BIX	FI	References
Northwestern China	Seasonal snow	0.16-3.20 (1.21)	0.44-1.47 (0.76)	1.20-1.92 (1.42)	This study
Tibetan Plateau	Cryoconite in glaciers	1.11-1.37 (1.27)	0.65-0.93 (0.80)	3.12-3.44 (3.24)	Feng et al., 2016
Yungui Plateau, China	Inland lakes	0.23-6.00 (1.57)	0.60-1.54 (0.93)	1.14-1.80 (1.37)	Zhang et al., 2010
Frasassi Caves, Italy	Cave water	1.79-3.28 (2.32)	0.80-1.12 (0.95)	~1.8	Birdwell and Engel, 2010
Springs in USA	Spring water	0.36-1.21 (0.76)	0.64-1.13 (0.87)	1.92-2.28 (2.09)	Birdwell and Engel, 2010
Gironde Estuary, France	Estuary	~4-17	0.6-0.8	1.14-1.22	Huguet et al., 2009
North Pacific Ocean	Ocean water	0.92-1.80 (1.49)	0.88-1.38 (1.0)	1.54-1.77 (1.66)	Helms et al., 2013
Tai Mountain, China	Fog water	3.23-6.79 (4.8)	0.64-1.02 (0.87)	1.42-1.83 (1.63)	Birdwell and Valsaraj, 2010
Jianghan Plain, China	Ground water	2.71-7.49	0.88-0.97	-	Huang et al., 2015
Colorado, USA	Aerosol in alpine sites	0.72-4.75 (2.42)	0.54-0.75 (0.65)	1.18-1.57 (1.4)	Xie et al., 2016
Granada, Spain	Urban aerosol	2.79-4.89	-	1.48-1.64	Mladenov et al., 2011

Table 4. Pearson's correlation coefficients (r) of major ions and F_{max} for fluorescent components when excluding data from site 67; the results for the entire dataset are shown in parentheses. Note: * denotes p<0.001.

	SO_4^{2-}	NO_3^-	nss-ndust-K^+
F_{max}(C1)	0.01 (0.14)	-0.10 (-0.04)	0.23 (0.48)
F_{max}(C2)	0.70* (0.72)	0.60* (0.57)	0.57* (0.69)
F_{max}(C3)	0.44 (0.42)	0.34 (0.23)	0.29 (0.68)

References

Anastasio, C., and Robles, T.: Light absorption by soluble chemical species in Arctic and Antarctic snow, J. Geophys. Res.-Atmos., 112, D24304, doi:10.1029/2007JD008695, 2007.

Anesio, A. M., Hodson, A. J., Fritz, A., Psenner, R., and Sattler, B.: High microbial activity on glaciers: importance to the global carbon cycle, Global Change Biol., 15, 955-960, 2009.

Antony, R., Grannas, A. M., Willoughby, A. S., Sleighter, R. L., Thamban, M., and Hatcher, P. G.: Origin and Sources of Dissolved Organic Matter in Snow on the East Antarctic Ice Sheet, Environ. Sci. Technol., 48, 6151-6159, 2014.

Bahram, M., Bro, R., Stedmon, C., and Afkhami, A.: Handling of Rayleigh and Raman scatter for PARAFAC modeling of fluorescence data using interpolation, J. Chemometr., 20, 99-105, 2006.

Beine, H., Anastasio, C., Esposito, G., Patten, K., Wilkening, E., Domine, F., Voisin, D., Barret, M., Houdier, S., and Hall, S.: Soluble, light-absorbing species in snow at Barrow, Alaska, J. Geophys. Res.-Atmos., 116, D00R05, doi:10.1029/2011JD016181, 2011.

Bhatia, M. P., Das, S. B., Longnecker, K., Charette, M. A., and Kujawinski, E. B.: Molecular characterization of dissolved organic matter associated with the Greenland ice sheet, Geochim. Cosmochim. Ac., 74, 3768-3784, 2010.

Birdwell, J. E., and Engel, A. S.: Characterization of dissolved organic matter in cave and spring waters using UV-Vis absorbance and fluorescence spectroscopy, Org. Geochem., 41, 270-280, 2010.

Birdwell, J. E., and Valsaraj, K. T.: Characterization of dissolved organic matter in fogwater by excitation-emission matrix fluorescence spectroscopy, Atmos. Environ., 44, 3246-3253, 2010.

Bond, T. C.: Spectral dependence of visible light absorption by carbonaceous particles emitted from coal combustion, Geophys. Res. Lett., 28, 4075-4078, 2001.

Bricaud, A., Morel, A., and Prieur, L.: ABSORPTION BY DISSOLVED ORGANIC-MATTER OF THE SEA (YELLOW SUBSTANCE) IN THE UV AND VISIBLE DOMAINS, Limnol. Oceanogr., 26, 43-53, 1981.

Bro, R.: PARAFAC. Tutorial and applications, Chemometr. Intell. Lab., 38, 149-171, 1997.

Chen, Q. C., Miyazaki, Y., Kawamura, K., Matsumoto, K., Coburn, S., Volkamer, R., Iwamoto, Y., Kagami, S., Deng, Y. G., Ogawa, S., Ramasamy, S., Kato, S., Ida, A., Kajii, Y., and Mochida, M.: Characterization of Chromophoric Water-Soluble Organic Matter in Urban, Forest, and Marine Aerosols by HR-ToF-AMS Analysis and Excitation Emission Matrix Spectroscopy, Environ. Sci. Technol., 50, 10351-10360, 2016.

Coble, P. G.: Characterization of marine and terrestrial DOM in seawater using excitation emission matrix spectroscopy, Mar. Chem., 51, 325-346, 1996.

Coble, P. G., Del Castillo, C. E., and Avril, B.: Distribution and optical properties of CDOM in the Arabian Sea during the 1995 Southwest Monsoon, Deep-Sea Res.

Pt. II, 45, 2195-2223, 1998.

Dang, C., and Hegg, D. A.: Quantifying light absorption by organic carbon in Western North American snow by serial chemical extractions, J. Geophys. Res.-Atmos., 119, doi:10.1002/2014JD022156, 2014.

Del Castillo, C. E., and Coble, P. G.: Seasonal variability of the colored dissolved organic matter during the 1994-95 NE and SW Monsoons in the Arabian Sea, Deep-Sea Res. Pt. II, 47, 1563-1579, 2000.

Doherty, S. J., Warren, S. G., Grenfell, T. C., Clarke, A. D., and Brandt, R. E.: Light-absorbing impurities in Arctic snow, Atmos. Chem. Phys., 10, 11647-11680, 2010.

Doherty, S. J., Grenfell, T. C., Forsstrom, S., Hegg, D. L., Brandt, R. E., and Warren, S. G.: Observed vertical redistribution of black carbon and other insoluble light-absorbing particles in melting snow, J. Geophys. Res.-Atmos., 118, 5553-5569, 2013.

Doherty, S. J., Dang, C., Hegg, D. A., Zhang, R. D., and Warren, S. G.: Black carbon and other light-absorbing particles in snow of central North America, J. Geophys. Res.-Atmos., 119, 12807-12831, 2014.

Doherty, S. J., Steele, M., Rigor, I., and Warren, S. G.: Interannual variations of light-absorbing particles in snow on Arctic sea ice, J. Geophys. Res.-Atmos., 120, 11391-11400, 2015.

Domine, F., Bock, J., Voisin, D., and Donaldson, D. J.: Can We Model Snow Photochemistry? Problems with the Current Approaches, J. Phys. Chem. A, 117, 4733-4749, 2013.

Duarte, R. M. B. O., Pio, C. A., and Duarte, A. C.: Synchronous scan and excitation-emission matrix fluorescence spectroscopy of water-soluble organic compounds in atmospheric aerosols, J. Atmos. Chem., 48, 157-171, 2004.

Dubnick, A., Barker, J., Sharp, M., Wadham, J., Lis, G., Telling, J., Fitzsimons, S., and Jackson, M.: Characterization of dissolved organic matter (DOM) from glacial environments using total fluorescence spectroscopy and parallel factor analysis, Ann. Glaciol., 51, 111-122, 2010.

Fellman, J. B., D'Amore, D. V., and Hood, E.: An evaluation of freezing as a preservation technique for analyzing dissolved organic C, N and P in surface water samples, Sci. Total Environ., 392, 305-312, 2008.

Feng, L., Xu, J. Z., Kang, S. C., Li, X. F., Li, Y., Jiang, B., and Shi, Q.: Chemical Composition of Microbe-Derived Dissolved Organic Matter in Cryoconite in Tibetan Plateau Glaciers: Insights from Fourier Transform Ion Cyclotron Resonance Mass Spectrometry Analysis, Environ. Sci. Technol., 50, 13215-13223, 2016.

Feng, L., An, Y., Xu, J., Kang, S., Li, X., Zhou, Y., Zhang, Y., Jiang, B., and Liao, Y.: Physical and chemical evolution of dissolved organic matter across the ablation season on a glacier in the central Tibetan Plateau, Biogeosciences Discuss., doi:10.5194/bg-2017-507, 2017.

Fichot, C. G., and Benner, R.: The spectral slope coefficient of chromophoric dissolved organic matter (S275-295) as a tracer of terrigenous dissolved organic carbon in river-influenced ocean margins, Limnol. Oceanogr., 57, 1453-1466, 2012.

Graber, E. R., and Rudich, Y.: Atmospheric HULIS: How humic-like are they? A comprehensive and critical review, Atmos. Chem. Phys., 6, 729-753, 2006.

Hadley, O. L., and Kirchstetter, T. W.: Black-carbon reduction of snow albedo, Nat. Clim. Change, 2, 437-440, 2012.

Hansen, A. M., Kraus, T. E. C., Pellerin, B. A., Fleck, J. A., Downing, B. D., and Bergamaschi, B. A.: Optical properties of dissolved organic matter (DOM): Effects of biological and photolytic degradation, Limnol. Oceanogr., 61, 1015-1032, 2016.

Hara, K., Osada, K., Kido, M., Hayashi, M., Matsunaga, K., Iwasaka, Y., Yamanouchi, T., Hashida, G., and Fukatsu, T.: Chemistry of sea-salt particles and inorganic halogen species in Antarctic regions: Compositional differences between coastal and inland stations, J. Geophys. Res.-Atmos., 109, D20208, doi:10.1029/2004JD004713, 2004.

Hecobian, A., Zhang, X., Zheng, M., Frank, N., Edgerton, E. S., and Weber, R. J.: Water-Soluble Organic Aerosol material and the light-absorption characteristics of aqueous extracts measured over the Southeastern United States, Atmos. Chem. Phys., 10, 5965-5977, 2010.

Hegg, D. A., Warren, S. G., Grenfell, T. C., Sarah, J. D., and Clarke, A. D.: Sources of light-absorbing aerosol in arctic snow and their seasonal variation, Atmos. Chem. Phys., 10, 10923-10938, 2010.

Helms, J. R., Stubbins, A., Ritchie, J. D., Minor, E. C., Kieber, D. J., and Mopper, K.: Absorption spectral slopes and slope ratios as indicators of molecular weight, source, and photobleaching of chromophoric dissolved organic matter, Limnol. Oceanogr., 53, 955-969, 2008.

Helms, J. R., Stubbins, A., Perdue, E. M., Green, N. W., Chen, H., and Mopper, K.: Photochemical bleaching of oceanic dissolved organic matter and its effect on absorption spectral slope and fluorescence, Mar. Chem., 155, 81-91, 2013.

Hill, V. J., and Zimmerman, R. C.: Characteristics of colored dissolved organic material in first year landfast sea ice and the underlying water column in the Canadian Arctic in the early spring, Mar. Chem., 180, 1-13, 2016.

Hood, E., Fellman, J., Spencer, R. G. M., Hernes, P. J., Edwards, R., D'Amore, D., and Scott, D.: Glaciers as a source of ancient and labile organic matter to the marine environment, Nature, 462, 1044-1047, 2009.

Hood, E., Battin, T. J., Fellman, J., O'Neel, S., and Spencer, R. G. M.: Storage and release of organic carbon from glaciers and ice sheets, Nat. Geosci., 8, 91-96, 2015.

Huang, J. P., Fu, Q. A., Zhang, W., Wang, X., Zhang, R. D., Ye, H., and Warren, S. G.: Dust And Black Carbon In Seasonal Snow across Northern China, B. Am. Meteorol. Soc., 92, 175-181, 2011.

Huang, S. B., Wang, Y. X., Ma, T., Tong, L., Wang, Y. Y., Liu, C. R., and Zhao, L.: Linking groundwater dissolved organic matter to sedimentary organic matter from a fluvio-lacustrine aquifer at Jianghan Plain, China by EEM-PARAFAC and hydrochemical analyses, Sci. Total Environ., 529, 131-139, 2015.

Huguet, A., Vacher, L., Relexans, S., Saubusse, S., Froidefond, J. M., and Parlanti, E.: Properties of fluorescent dissolved organic matter in the Gironde Estuary, Org. Geochem., 40, 706-719, 2009.

IPCC: Climate Change 2013: The Physical Science Basis. Contribution of Working Group I to the Fifth Assessment Report of the Intergovernmental Panel on Climate Change, edited by: Stocker, T. F., Qin, D., Plattner, G.-K., Tignor, M., Allen, S. K., Boschung, J., Nauels, A., Xia, Y., Bex, V., and Midgley, P. M., Cambridge University Press, Cambridge, United Kingdom and New York, NY, USA, 1535 pp., 2013.

Jones, H. G.: The ecology of snow-covered systems: a brief overview of nutrient cycling and life in the cold, Hydrol. Process. 13, 2135-2147, 1999.

Kothawala, D. N., Murphy, K. R., Stedmon, C. A., Weyhenmeyer, G. A., and Tranvik, L. J.: Inner filter correction of dissolved organic matter fluorescence, Limnol. Oceanogr.-Meth, 11, 616-630, 2013.

Lawaetz, A. J., and Stedmon, C. A.: Fluorescence Intensity Calibration Using the Raman Scatter Peak of Water, Appl. Spectrosc., 63, 936-940, 2009.

Lawson, E. C., Wadham, J. L., Tranter, M., Stibal, M., Lis, G. P., Butler, C. E. H., Laybourn-Parry, J., Nienow, P., Chandler, D., and Dewsbury, P.: Greenland Ice Sheet exports labile organic carbon to the Arctic oceans, Biogeosciences, 11, 4015-4028, 2014.

Lee, H. J., Laskin, A., Laskin, J., and Nizkorodov, S. A.: Excitation-Emission Spectra and Fluorescence Quantum Yields for Fresh and Aged Biogenic Secondary Organic Aerosols, Environ. Sci. Technol., 47, 5763-5770, 2013.

Liu, Y. Q., Yao, T. D., Jiao, N. Z., Kang, S. C., Xu, B. Q., Zeng, Y. H., Huang, S. J., and Liu, X. B.: Bacterial diversity in the snow over Tibetan Plateau Glaciers, Extremophiles, 13, 411-423, 2009.

Lutz, S., Anesio, A. M., Raiswell, R., Edwards, A., Newton, R. J., Gill, F., and Benning, L. G.: The biogeography of red snow microbiomes and their role in melting arctic glaciers, Nat. Commun., 7, doi:10.1038/ncomms11968, 2016.

Massicotte, P., Asmala, E., Stedmon, C., and Markager, S.: Global distribution of dissolved organic matter along the aquatic continuum: Across rivers, lakes and oceans, Sci. Total Environ. , 609, 180-191, 2017.

McKnight, D. M., Boyer, E. W., Westerhoff, P. K., Doran, P. T., Kulbe, T., and Andersen, D. T.: Spectrofluorometric characterization of dissolved organic matter for indication of precursor organic material and aromaticity, Limnol. Oceanogr., 46, 38-48, 2001.

Mladenov, N., Alados-Arboledas, L., Olmo, F. J., Lyamani, H., Delgado, A., Molina, A., and Reche, I.: Applications of optical spectroscopy and stable isotope analyses to organic aerosol source discrimination in an urban area, Atmos. Environ. , 45, 1960-1969, 2011.

Mladenov, N., Williams, M. W., Schmidt, S. K., and Cawley, K.: Atmospheric deposition as a source of carbon and nutrients to an alpine catchment of the Colorado Rocky Mountains, Biogeosciences, 9, 3337-3355, 2012.

Murphy, K. R., Stedmon, C. A., Waite, T. D., and Ruiz, G. M.: Distinguishing between terrestrial and autochthonous organic matter sources in marine environments using fluorescence spectroscopy, Mar. Chem., 108, 40-58, 2008.

Murphy, K. R., Hambly, A., Singh, S., Henderson, R. K., Baker, A., Stuetz, R., and

Khan, S. J.: Organic Matter Fluorescence in Municipal Water Recycling Schemes: Toward a Unified PARAFAC Model, Environ. Sci. Technol., 45, 2909-2916, 2011.

Murphy, K. R., Stedmon, C. A., Graeber, D., and Bro, R.: Fluorescence spectroscopy and multi-way techniques. PARAFAC, Anal. Methods-Uk., 5, 6557-6566, 2013.

Niu, H. W., Kang, S. C., Lu, X. X., and Shi, X. F.: Distributions and light absorption property of water soluble organic carbon in a typical temperate glacier, southeastern Tibetan Plateau, Tellus B, 70, 1445379, 10.1080/16000889.2018.1468705, 2018.

Oh, M. S., Lee, T. J., and Kim, D. S.: Quantitative Source Apportionment of Size-segregated Particulate Matter at Urbanized Local Site in Korea, Aerosol Air Qual. Res., 11, 247-264, 2011.

Otero, M., Mendonca, A., Valega, M., Santos, E. B. H., Pereira, E., Esteves, V. I., and Duarte, A.: Fluorescence and DOC contents of estuarine pore waters from colonized and non-colonized sediments: Effects of sampling preservation, Chemosphere, 67, 211-220, 2007.

Peacock, M., Freeman, C., Gauci, V., Lebron, I., and Evans, C. D.: Investigations of freezing and cold storage for the analysis of peatland dissolved organic carbon (DOC) and absorbance properties, Environ. Sci-Proc Imp., 17, 1290-1301, 2015.

Pegau, W. S.: Inherent optical properties of the central Arctic surface waters, J. Geophys. Res.-Oceans, 107(C10), 8035, doi:10.1029/2000JC000382, 2002.

Pio, C. A., Legrand, M., Oliveira, T., Afonso, J., Santos, C., Caseiro, A., Fialho, P., Barata, F., Puxbaum, H., Sanchez-Ochoa, A., Kasper-Giebl, A., Gelencser, A., Preunkert, S., and Schock, M.: Climatology of aerosol composition (organic versus inorganic) at nonurban sites on a west-east transect across Europe, J. Geophys. Res.-Atmos., 112, D23S02, doi:10.1029/2006JD008038, 2007.

Pu, W., Wang, X., Wei, H. L., Zhou, Y., Shi, J. S., Hu, Z. Y., Jin, H. C., and Chen, Q. L.: Properties of black carbon and other insoluble light-absorbing particles in seasonal snow of northwestern China, The Cryosphere, 11, 1213-1233, 2017.

Seekell, D. A., Lapierre, J. F., Ask, J., Bergstrom, A. K., Deininger, A., Rodriguez, P., and Karlsson, J.: The influence of dissolved organic carbon on primary production in northern lakes, Limnol. Oceanogr., 60, 1276-1285, 2015.

Singer, G. A., Fasching, C., Wilhelm, L., Niggemann, J., Steier, P., Dittmar, T., and Battin, T. J.: Biogeochemically diverse organic matter in Alpine glaciers and its downstream fate, Nat. Geosci., 5, 710-714, 2012.

Spencer, R. G. M., Butler, K. D., and Aiken, G. R.: Dissolved organic carbon and chromophoric dissolved organic matter properties of rivers in the USA, J. Geophys. Res.-Biogeo., 117, G03001, doi:10.1029/2011JG001928, 2012.

Stedmon, C. A., Markager, S., and Bro, R.: Tracing dissolved organic matter in aquatic environments using a new approach to fluorescence spectroscopy, Mar. Chem., 82, 239-254, 2003.

Stedmon, C. A., and Markager, S.: Tracing the production and degradation of autochthonous fractions of dissolved organic matter by fluorescence analysis, Limnol. Oceanogr., 50, 1415-1426, 2005a.

Stedmon, C. A., and Markager, S.: Resolving the variability in dissolved organic matter

fluorescence in a temperate estuary and its catchment using PARAFAC analysis, Limnol. Oceanogr., 50, 686-697, 2005b.

Stedmon, C. A., and Bro, R.: Characterizing dissolved organic matter fluorescence with parallel factor analysis: a tutorial, Limnol. Oceanogr.-Meth., 6, 572-579, 2008.

Stein, A. F., Draxler, R. R., Rolph, G. D., Stunder, B. J. B., Cohen, M. D., and Ngan, F.: Noaa's Hysplit Atmospheric Transport and Dispersion Modeling System, B. Am. Meteorol. Soc., 96, 2059-2077, 2015.

Stubbins, A., Hood, E., Raymond, P. A., Aiken, G. R., Sleighter, R. L., Hernes, P. J., Butman, D., Hatcher, P. G., Striegl, R. G., Schuster, P., Abdulla, H. A. N., Vermilyea, A. W., Scott, D. T., and Spencer, R. G. M.: Anthropogenic aerosols as a source of ancient dissolved organic matter in glaciers, Nat. Geosci., 5, 198-201, 2012.

Thieme, L., Graeber, D., Kaupenjohann, M., and Siemens, J.: Fast-freezing with liquid nitrogen preserves bulk dissolved organic matter concentrations, but not its composition, Biogeosciences, 13, 4697-4705, 2016.

Thrane, J.-E., Hessen, D. O., and Andersen, T.: The Absorption of Light in Lakes: Negative Impact of Dissolved Organic Carbon on Primary Productivity, Ecosystems, 17, 1040-1052, 2014.

Twardowski, M. S., Boss, E., Sullivan, J. M., and Donaghay, P. L.: Modeling the spectral shape of absorption by chromophoric dissolved organic matter, Mar. Chem., 89, 69-88, 2004.

Vaehaetalo, A. V., and Wetzel, R. G.: Photochemical and microbial decomposition of chromophoric dissolved organic matter during long (months-years) exposures, Mar. Chem., 89, 313-326, 2004.

Voisin, D., Jaffrezo, J. L., Houdier, S., Barret, M., Cozic, J., King, M. D., France, J. L., Reay, H. J., Grannas, A., Kos, G., Ariya, P. A., Beine, H. J., and Domine, F.: Carbonaceous species and humic like substances (HULIS) in Arctic snowpack during OASIS field campaign in Barrow, J. Geophys. Res.-Atmos., 117, D00R19, doi:10.1029/2011JD016612, 2012.

Wang, H. L., Zhuang, Y. H., Wang, Y., Sun, Y., Yuan, H., Zhuang, G. S., and Hao, Z. P.: Long-term monitoring and source apportionment of PM2.5/PM10 in Beijing, China, J. Environ. Sci-China, 20, 1323-1327, 2008.

Wang, X., Doherty, S. J., and Huang, J.: Black carbon and other light - absorbing impurities in snow across Northern China, J. Geophys. Res.-Atmos., 118, 1471-1492, 2013.

Wang, X., Pu, W., Zhang, X. Y., Ren, Y., and Huang, J. P.: Water-soluble ions and trace elements in surface snow and their potential source regions across northeastern China, Atmos. Environ., 114, 57-65, 2015.

Wang, X., Pu, W., Ren, Y., Zhang, X., Zhang, X., Shi, J., Jin, H., Dai, M., and Chen, Q.: Observations and model simulations of snow albedo reduction in seasonal snow due to insoluble light-absorbing particles during 2014 Chinese survey, Atmos. Chem. Phys., 17, 2279-2296, 2017.

Wang, Y., Zhuang, G. S., Zhang, X. Y., Huang, K., Xu, C., Tang, A. H., Chen, J. M.,

and An, Z. S.: The ion chemistry, seasonal cycle, and sources of PM2.5 and TSP aerosol in Shanghai, Atmos. Environ., 40, 2935-2952, 2006.

Wang, Y. H., Xu, Y. P., Spencer, R. G. M., Zito, P., Kellerman, A., Podgorski, D., Xiao, W. J., Wei, D. D., Rashid, H., and Yang, Y. H.: Selective Leaching of Dissolved Organic Matter From Alpine Permafrost Soils on the Qinghai-Tibetan Plateau, J. Geophys. Res.-Biogeo., 123, 1005-1016, 2018.

Warren, S. G., and Wiscombe, W. J.: A Model for the Spectral Albedo of Snow .2. Snow Containing Atmospheric Aerosols, J. Atmos. Sci., 37, 2734-2745, 1980.

Xie, M. J., Mladenov, N., Williams, M. W., Neff, J. C., Wasswa, J., and Hannigan, M. P.: Water soluble organic aerosols in the Colorado Rocky Mountains, USA: composition, sources and optical properties, Sci. Rep.-Uk, 6, 39339, doi:10.1038/srep39339, 2016.

Yamashita, Y., Jaffe, R., Maie, N., and Tanoue, E.: Assessing the dynamics of dissolved organic matter (DOM) in coastal environments by excitation emission matrix fluorescence and parallel factor analysis (EEM-PARAFAC), Limnol. Oceanogr., 53, 1900-1908, 2008.

Yamashita, Y., Cory, R. M., Nishioka, J., Kuma, K., Tanoue, E., and Jaffe, R.: Fluorescence characteristics of dissolved organic matter in the deep waters of the Okhotsk Sea and the northwestern North Pacific Ocean, Deep-Sea Res. Pt. II, 57, 1478-1485, 2010.

Yan, F. P., Kang, S. C., Li, C. L., Zhang, Y. L., Qin, X., Li, Y., Zhang, X. P., Hu, Z. F., Chen, P. F., Li, X. F., Qu, B., and Sillanpaa, M.: Concentration, sources and light absorption characteristics of dissolved organic carbon on a medium-sized valley glacier, northern Tibetan Plateau, The Cryosphere, 10, 2611-2621, 2016.

Ye, H., Zhang, R. D., Shi, J. S., Huang, J. P., Warren, S. G., and Fu, Q.: Black carbon in seasonal snow across northern Xinjiang in northwestern China, Environ. Res. Lett., 7, 044002, doi:10.1088/1748-9326/7/4/044002, 2012.

Yu, H. R., Liang, H., Qu, F. S., Han, Z. S., Shao, S. L., Chang, H. Q., and Li, G. B.: Impact of dataset diversity on accuracy and sensitivity of parallel factor analysis model of dissolved organic matter fluorescence excitation-emission matrix, Sci. Rep.-Uk, 5, 10207, doi:10.1038/srep10207, 2015.

Zhang, R., Hegg, D. A., Huang, J., and Fu, Q.: Source attribution of insoluble light-absorbing particles in seasonal snow across northern China, Atmos. Chem. Phys., 13, 6091-6099, 2013.

Zhang, Y. L., van Dijk, M. A., Liu, M. L., Zhu, G. W., and Qin, B. Q.: The contribution of phytoplankton degradation to chromophoric dissolved organic matter (CDOM) in eutrophic shallow lakes: Field and experimental evidence, Water Res., 43, 4685-4697, 2009.

Zhang, Y. L., Zhang, E. L., Yin, Y., van Dijk, M. A., Feng, L. Q., Shi, Z. Q., Liu, M. L., and Qin, B. Q.: Characteristics and sources of chromophoric dissolved organic matter in lakes of the Yungui Plateau, China, differing in trophic state and altitude, Limnol. Oceanogr., 55, 2645-2659, 2010.

Zhang, Y. L., Yin, Y., Feng, L. Q., Zhu, G. W., Shi, Z. Q., Liu, X. H., and Zhang, Y. Z.: Characterizing chromophoric dissolved organic matter in Lake Tianmuhu and its

catchment basin using excitation-emission matrix fluorescence and parallel factor analysis, Water Res., 45, 5110-5122, 2011.

Zhao, Y., Song, K., Wen, Z., Li, L., Zang, S., Shao, T., Li, S., and Du, J.: Seasonal characterization of CDOM for lakes in semiarid regions of Northeast China using excitation–emission matrix fluorescence and parallel factor analysis (EEM–PARAFAC), Biogeosciences, 13, 1635-1645, 2016.

Zhou, Y., Wang, X., Wu, X., Cong, Z., Wu, G., and Ji, M.: Quantifying Light Absorption of Iron Oxides and Carbonaceous Aerosol in Seasonal Snow across Northern China, Atmosphere, 8, 63, doi:10.3390/atmos8040063, 2017.

Zhou, Y. Q., Yao, X. L., Zhang, Y. B., Shi, K., Zhang, Y. L., Jeppesen, E., Gao, G., Zhu, G. W., and Qin, B. Q.: Potential rainfall-intensity and pH-driven shifts in the apparent fluorescent composition of dissolved organic matter in rainwater, Environ. Pollut., 224, 638-648, 2017.

Zsolnay, A., Baigar, E., Jimenez, M., Steinweg, B., and Saccomandi, F.: Differentiating with fluorescence spectroscopy the sources of dissolved organic matter in soils subjected to drying, Chemosphere, 38, 45-50, 1999.